Monthly Notices of the ROYAL ASTRONOMICAL SOCIETY

MNRAS **498,** 3835–3851 (2020) doi:10.1093/mnras/staa2617
Advance Access publication 2020 August 27

SN 2014ab: an aspherical Type IIn supernova with low polarization

Christopher Bilinski,[1★] Nathan Smith,[1] G. Grant Williams,[2] Paul Smith,[1] Jennifer Andrews,[1] Kelsey I. Clubb,[3] WeiKang Zheng,[3] Alexei V. Filippenko,[3,4†] Ori D. Fox,[5] Griffin Hosseinzadeh,[6] D. Andrew Howell,[7,8] Patrick L. Kelly,[9] Peter Milne,[1] D. J. Sand,[1] Jennifer L. Hoffman,[10] Douglas C. Leonard,[11] Samantha Cargill,[3] Chadwick Casper,[3] Goni Halevy,[12] Haejung Kim,[13] Sahana Kumar,[3,14] Kenia Pina[3] and Heechan Yuk[3,15]

[1]*Steward Observatory, University of Arizona, 933 N. Cherry Avenue, Tucson, AZ 85721, USA*
[2]*MMT Observatory, Tucson, AZ 85721-0065, USA*
[3]*Department of Astronomy, University of California, Berkeley, CA 94720-3411, USA*
[4]*Miller Institute for Basic Research in Science, University of California, Berkeley, CA 94720, USA*
[5]*Space Telescope Science Institute, 3700 San Martin Drive, Baltimore, MD 21218, USA*
[6]*Center for Astrophysics | Harvard & Smithsonian, 60 Garden Street, Cambridge, MA 02138-1516, USA*
[7]*Department of Physics, University of California, Santa Barbara, CA 93106-9530, USA*
[8]*Las Cumbres Observatory, 6740 Cortona Drive Suite 102, Goleta, CA 93117-5575, USA*
[9]*School of Physics and Astronomy, University of Minnesota, 116 Church Street S. E., Minneapolis, MN 55455, USA*
[10]*Department of Physics & Astronomy, University of Denver, 2112 East Wesley Avenue, Denver, CO 80208, USA*
[11]*Department of Astronomy, San Diego State University, San Diego, CA 92812, USA*
[12]*Department of Astrophysical Sciences, Princeton University, 4 Ivy Lane, Princeton, NJ 08544, USA*
[13]*Dr. Opinion, 201 Dolores Avenue, San Leandro, CA 94577, USA*
[14]*Department of Physics, Florida State University, Tallahassee, FL 32306, USA*
[15]*Homer L. Dodge Department of Physics and Astronomy, The University of Oklahoma, Norman, OK 73019, USA*

Accepted 2020 August 20. Received 2020 August 18; in original form 2020 July 16

ABSTRACT

We present photometry, spectra, and spectropolarimetry of supernova (SN) 2014ab, obtained through ∼200 d after peak brightness. SN 2014ab was a luminous Type IIn SN ($M_V < -19.14$ mag) discovered after peak brightness near the nucleus of its host galaxy, VV 306c. Pre-discovery upper limits constrain the time of explosion to within 200 d prior to discovery. While SN 2014ab declined by ∼1 mag over the course of our observations, the observed spectrum remained remarkably unchanged. Spectra exhibit an asymmetric emission-line profile with a consistently stronger blueshifted component, suggesting the presence of dust or a lack of symmetry between the far side and near side of the SN. The Pa β emission line shows a profile very similar to that of H α, implying that this stronger blueshifted component is caused either through obscuration by large dust grains, occultation by optically thick material, or a lack of symmetry between the far side and near side of the interaction region. Despite these asymmetric line profiles, our spectropolarimetric data show that SN 2014ab has little detected polarization after accounting for the interstellar polarization. We are likely seeing emission from a photosphere that has only small deviation from circular symmetry in the plane normal to our line of sight, but with either large-grain dust or significant asymmetry in the density of circumstellar material or SN ejecta along our line of sight. We suggest that SN 2014ab and SN 2010jl (as well as other SNe IIn) may be events with similar geometry viewed from different directions.

Key words: polarization – supernovae: general – supernovae: individual: SN 2014ab.

1 INTRODUCTION

Type IIn supernovae (SNe IIn) are observed when fast SN ejecta crash into dense circumstellar material (CSM). Strong narrow and intermediate-width hydrogen emission lines indicate the presence of these CSM interaction regions (Schlegel 1990; Filippenko 1997; Smith 2017). Because SNe IIn are powered not only by emission from the SN ejecta, but also from CSM interaction, unraveling the geometry of the explosion can be complicated. In order to better understand both the shape of the SN ejecta and the CSM, two different approaches (spectroscopy and spectropolarimetry) are commonly used.

Spectral line profile shapes can help clarify the geometry of the CSM or SN ejecta. Blueshifted line profiles can arise when receding portions of the CSM or ejecta are extinguished by dust or occulted by the SN photosphere, while any type of line asymmetry might arise from an aspherical explosion or aspherical CSM. The spectra of SNe IIn often show signs of asphericity in the CSM and the SN ejecta revealed by line profiles (SN 1988Z: Chugai & Danziger 1994;

★ E-mail: cgbilinsk@gmail.com
† Miller Senior Fellow

Published by Oxford University Press on behalf of the Royal Astronomical Society

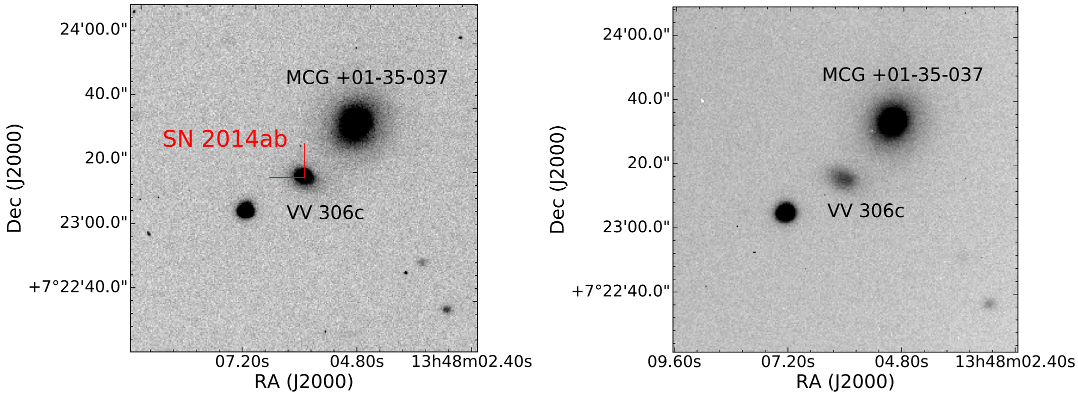

Figure 1. Left: *R*-band image of VV 306c, the host galaxy of SN 2014ab, taken with the Lick Nickel 1-m telescope with the SN present (day 72). The red cross hairs indicate the location of SN 2014ab. Right: *R*-band image of VV 306c taken with the Kuiper telescope after the SN had faded beyond detectability (day 893).

SN 1995N: Fransson et al. 2002; SN 1997eg: Hoffman et al. 2008; SN 1998S: Leonard et al. 2000; Wang et al. 2001; Fransson et al. 2005; Mauerhan & Smith 2012; SN 2005ip: Smith et al. 2009; Katsuda et al. 2014; SN 2006jd: Stritzinger et al. 2012; SN 2006tf: Smith et al. 2008; SN 2009ip: Mauerhan et al. 2014; Reilly et al. 2017; SN 2010jl: Smith et al. 2012; Fransson et al. 2014; PTF11iqb: Smith et al. 2015; SN 2012ab: Bilinski et al. 2018; SN 2013L: Andrews et al. 2017).

One can also use spectropolarimetric data to measure the polarization and position angle of integrated light. Although only a few SNe IIn have spectropolarimetric data published (SN 1997eg: Hoffman et al. 2008; SN 1998S: Leonard et al. 2000; SN 2006tf: Smith et al. 2008; SN 2010jl: Patat et al. 2011; SN 2009ip: Mauerhan et al. 2014; Reilly et al. 2017; SN 2012ab: Bilinski et al. 2018; SN 2017hcc: Kumar et al. 2019), every one observed so far has a high level of continuum polarization (1–3 per cent), seemingly indicating that strong asphericity is the standard for this class of objects. This conclusion may be biased if spectropolarimetric data of SNe IIn with low or undetected polarization go unpublished, of course.

In this paper, we analyse the Type IIn SN 2014ab. SN 2014ab was discovered by the Catalina Sky Survey (CSS) on 2014 March 9.43 (UT dates are used in this paper) at an apparent *V*-band magnitude of 16.4 ($M_V = -19.0$ mag) (Drake et al. 2009; Howerton et al. 2014), located in the galaxy VV 306c (redshift $z = 0.023203$; Vorontsov-Velyaminov 1959).[1] The SN is located at α(J2000) = $13^{\rm h}48^{\rm m}06\overset{\rm s}{.}05$, δ(J2000) = $+07^\circ23'16\overset{''}{.}12$. We adopt a Milky Way extinction along the line of sight of $A_V = 0.083$ mag ($E_{B-V} = 0.027$ mag; Schlafly & Finkbeiner 2011), and a redshift-based distance [which assumes $H_0 = 73\,{\rm km\,s^{-1}\,Mpc^{-1}}$ (Riess et al. 2005) and takes into account influences from the Virgo cluster, the Great Attractor, and the Shapley supercluster] of 105.7 ± 7.4 Mpc from the NASA/IPAC Extragalactic Database.[2] *R*-band images with and without the SN are shown in Fig. 1. An infrared (IR) spectrum acquired with the 6.5-m Magellan Baade Telescope at Las Campanas Observatory with the Folded-port Infrared Echellette (FIRE; 800–2500 nm) on 2014 March 10.25 revealed features indicative of an SN IIn more than a month past maximum brightness (Howerton et al. 2014). Additionally, a visual-wavelength spectrum (3985–9315 Å, 18 Å resolution) was obtained by the Public ESO Spectroscopic Survey for Transient Objects (PESSTO) with the ESO New Technology Telescope at La Silla on 2014 March 9 using the EFOSC2 and Grism 13 (Fraser et al. 2014). PESSTO reports a Type IIn classification with narrow Balmer emission lines, shallow and broad P-Cygni absorption, broad Ca near-IR triplet emission, and broad P-Cygni Na I D (Fraser et al. 2014). Here, we present results for SN 2014ab based on five epochs of spectropolarimetry, 31 epochs of spectroscopy, and photometry spanning 4039 d.

As our paper was in the final stage of preparation, an independent analysis of photometry and spectra of the same SN appeared in a preprint (Moriya et al. 2020). We briefly comment on similarities and differences between our analysis and that of Moriya et al. (2020) in the final section of this paper.

2 OBSERVATIONS

2.1 Explosion date and pre-SN activity

Unfortunately, SN 2014ab was discovered after peak brightness and the explosion date is poorly constrained. Pre-discovery CSS imaging of the host galaxy of SN 2014ab places rough limits on the pre-explosion activity and the explosion date. The object was detected in CSS images 56 d prior to the discovery announcement image. We use this CSS detection date (2014 January 12.4755, MJD = 56669.4755) as the true discovery date of SN 2014ab and adopt this as day 0 throughout our analysis. CSS images of the region were taken spanning 3203 d before discovery up until 836 d after discovery (Fig. 2), with no indication of any other transient events (i.e. no precursor outbursts; see Bilinski et al. 2015) occurring at the location of the SN. The brightest observed magnitude ($m_V = 15.84$, $M_V = -19.54$ mag) occurred in the CSS image taken 56 d prior to the discovery announcement image. CSS images taken 212 d prior to the discovery announcement image show no detection of the transient, and we have no photometry at the location of the SN between days −212 and 0. It is during this time period that the explosion occurred, most likely at least tens of days before discovery.

2.2 Photometry

We retrieved the *V*-band light curve from the CSS that spans a total of 4039 d, shown in Fig. 2. As this light curve is not template

[1]We note that the host galaxy is named VV 306c according to the SIMBAD data base. Moriya et al. (2020) stated that the host galaxy of SN 2014ab is MCG + 01-35-037, but this galaxy is the larger one located ∼20 arcsec to the north-west (see Fig. 1).

[2]The NASA/IPAC Extragalactic Database (NED) is operated by the Jet Propulsion Laboratory, California Institute of Technology, under contract with the National Aeronautics and Space Administration (NASA; http://ned.ipac.caltech.edu).

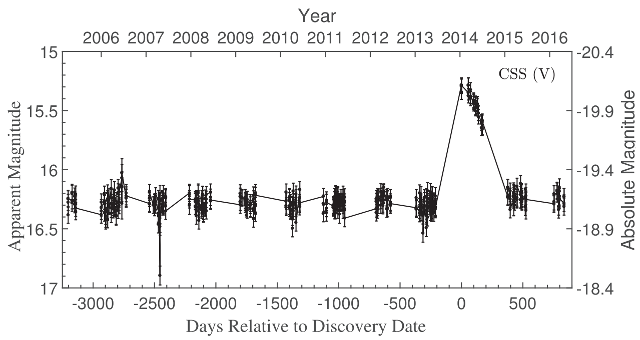

Figure 2. The full range of CSS unfiltered (similar to *V*-band) photometric observations of SN 2014ab with light from its host galaxy, VV 306c, included in the aperture. No pre-SN outburst is evident in these data. The black line connecting the photometric observations is included to guide the eye and does not reflect any sort of model.

subtracted, it includes significant amounts of host-galaxy light. We estimate the median flux in the host galaxy in the CSS images when no SN is present and subtract this host flux from the rest of the CSS light curve to estimate the SN flux. The shape of the resulting light curve is very similar to our 1-m Nickel telescope (at Lick Observatory) *V*-band light curve, though the fact that the CSS light curve suggests a systematically brighter SN is likely due to residual contamination from the host galaxy and the size of the region upon which photometry was performed. We also obtained a late-time (day 893) *V*-band image of the host galaxy (shown in Fig. 1) with the Mont4K CCD Imager on the Kuiper telescope.

B, *V*, *R*, and *I* images of SN 2014ab obtained with the Nickel telescope were reduced using a custom pipeline (Ganeshalingam et al. 2010). Image-subtraction procedures performed by the ISIS package (Alard & Lupton 1998) were applied in order to remove the host-galaxy light, using template images obtained on 2016 January 26, after the SN had faded below our detection limit. Point spread function (PSF) photometry was then obtained using DAOPHOT (Stetson 1987) from the IDL Astronomy User's Library.[3] Several nearby stars were chosen from the SDSS catalogue for calibrating Nickel data. Their magnitudes were first transformed into the Landolt system using the empirical prescription presented by Robert Lupton,[4] then transformed to the Nickel natural system. Apparent magnitudes were all measured in the Nickel natural system, and the final results were transformed to the standard system using local calibrators and colour terms of 'Nickel2' (see table 1 from Stahl et al. 2019). We display the Nickel telescope light curve in Fig. 3 alongside an additional unfiltered (similar to *V*-band) light curve from the CSS.

2.3 Spectroscopy

We obtained optical spectra with a variety of telescopes instruments over the course of ∼200 d after the detection of SN 2014ab. Our 36 spectra were taken on 34 different nights with the Kast double spectrograph (Miller & Stone 1993) on the Shane 3-m telescope at Lick Observatory; EFOSC2 on the 3.58-m ESO-NTT (Buzzoni et al. 1984); X-shooter on the 8.2-m VLT (Vernet et al. 2011); the FLOYDS spectrograph on the 2-m Las Cumbres Observatory telescopes as part of the LCO Supernova Key Project (Brown et al. 2013); the Bluechannel (BC) Spectrograph on the 6.5-m Multiple Mirror Telescope (MMT); and the Spectropolarimeter (SPOL) on the 1.54-m Kuiper telescope, the 2.3-m Bok telescope, and the 6.5-m MMT. All spectra were taken with the long slit at the parallactic angle (Filippenko 1982). The spectroscopic observations are detailed in Table 1.

Standard spectral reduction procedures were followed for all of the spectra (except SPOL polarization data; see Section 2.4). The reduced optical spectra are shown in Fig. 4. While we focus our analysis on the optical spectra, the X-shooter spectra also contain near-IR data, plotted in Fig. 5.

2.4 Spectropolarimetry

Spectropolarimetric observations of SN 2014ab were obtained using the CCD Imaging/SPOL (Schmidt, Stockman & Smith 1992) on the 2.3-m Bok, 1.54-m Kuiper, and 6.5-m MMT telescopes. A 5 arcsec slit was used at the Bok and Kuiper telescopes, while a 3 arcsec slit was used at the MMT. Observation and data reduction procedures were followed as in Bilinski et al. 2018, except using a wavelength range of 4000–7550 Å. Nine q and u sequences were acquired at the Bok telescope, 11 at the Kuiper telescope, and two at the MMT. Each set of sequences was then combined by epoch for a higher signal-to-noise ratio.

Hiltner 960 and VI Cyg 12 were used as polarimetric standards (Schmidt, Elston & Lupie 1992) to obtain the instrumental polarization angle for SPOL at the Bok and MMT telescopes. The discrepancy between the measured and the expected position angle was $<0.2^{\circ}$ for each of the polarimetric standard stars. BD + 28°4211 was used as an unpolarized flux standard to ensure that the instrumental polarization for SPOL was <0.1 per cent for each epoch (Oke 1990). We also use unpublished spectropolarimetry of SN 2010jl (Williams et al., in preparation) obtained by the SN Spectropolarimetry Project to compare to our spectropolarimetry of SN 2014ab.

3 RESULTS

3.1 Extinction and reddening

We use the strength of Na I D absorption to evaluate the local reddening along the line of sight to SN 2014ab within its host galaxy. The strength of the narrow absorption lines of Na I D λλ5890 (D2), 5896 (D1) correlates with the interstellar dust extinction present along a particular line of sight. While this relation does not perform well with low-resolution spectra (Poznanski et al. 2011), it can be used with moderate-resolution spectra when the Na I D2 line is not saturated and the doublet is not blended (Poznanski, Prochaska & Bloom 2012). Phillips et al. (2013) found that the sodium doublet absorption for one-fourth of their sample of SNe Ia was stronger than expected for dust-extinction values estimated from SN colour. In our moderately high-resolution (R = 3500) spectrum on day 70, we measure the equivalent widths for the D1 and D2 lines (λ5896 and λ5890, respectively, in the host-galaxy rest frame) to be 0.21 ± 0.03 Å and 0.31 ± 0.03 Å, respectively (see Fig. 6). Based on these equivalent widths, the relation provided by Poznanski et al. (2012) suggests that we have additional extinction along the line of sight caused by the host galaxy of $A_V \approx 0.18$ mag (assuming $A_V = 3.08\, E_{B-V}$; Pei 1992) or $A_R \approx 0.14$ mag.[5] If we choose the model (described in Footnote 5) with the highest estimated extinction, we

[3] http://idlastro.gsfc.nasa.gov/
[4] http://www.sdss.org/dr7/algorithms/sdssUBVRITransform.html#Lupton2005

[5] Other attempts have been made to connect the equivalent width of the absorption in the sodium doublet to extinction (Richmond et al. 1994; Munari & Zwitter 1997; Turatto, Benetti & Cappellaro 2003; Poznanski et al. 2012).

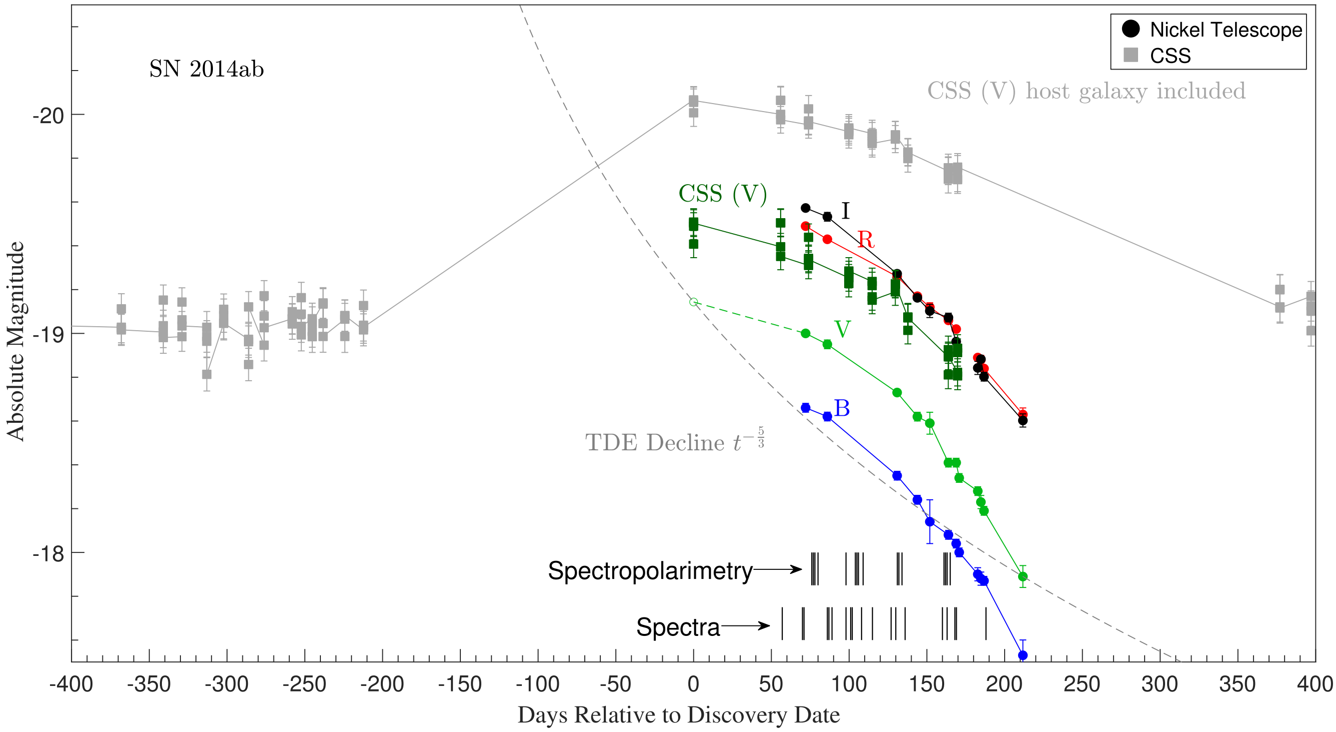

Figure 3. Photometric observations of SN 2014ab taken by the Lick Nickel 1-m telescope (*BVRI*) and the CSS (unfiltered, but similar to *V* band). CSS data that include host-galaxy light (from Fig. 2) are shown in grey, while host-flux-subtracted CSS unfiltered measurements are shown in dark green. Nickel *V*-band data do not extend back to the discovery date, so we have shown a projected peak magnitude value (based on extrapolating the shape of the CSS unfiltered light curve) with an unfilled green circle connected by a green dotted line. The expected decline rate for a tidal disruption event (TDE) with an explosion date of −212 is shown as a dotted grey line. Dates on which we also obtained spectra and spectropolarimetry are marked by black dashes. Dates are relative to the adopted discovery date of 2014 January 12.4755.

would have $A_V = 0.55$ mag instead. We adopt a total Milky Way (Schlafly & Finkbeiner 2011) plus host-galaxy extinction of $A_V = 0.26$ mag ($E_{B-V} = 0.083$ mag) or $A_R = 0.21$ mag. Fig. 4 shows spectra dereddened by $E_{B-V} = 0.083$ mag.

3.2 Light curve

Fig. 3 shows the light curve of SN 2014ab obtained by the Nickel telescope and CSS. The absolute magnitudes shown have been adjusted for Milky Way and host-galaxy reddening (determined from Na I D line strengths as discussed in Section 3.1) and for the distance modulus of $\mu = 35.1$ mag based on a distance to the host galaxy of 105.7 ± 7.4 Mpc.

CSS photometry of the host galaxy prior to the initial discovery announcement suggests that SN 2014ab initially brightened sometime between days −212 and 0 relative to the discovery date. We measure SN 2014ab to have the brightest observed magnitude at $M_V = -19.54$ mag on the first CSS detection date, so the peak luminosity may have occurred sometime before then. Even our earliest spectra resemble those of SN 2010jl (Smith et al. 2012) more than 50 d after peak, suggesting that SN 2014ab was already well past maximum brightness when discovered. For this reason, all dates are cited relative to the CSS first detection date, which may be several weeks or months after the SN exploded.

Because the CSS photometry included host-galaxy light and is unfiltered rather than true *V*-band data, we favour using the Nickel data for a constraint on the peak *V*-band magnitude. Specifically, we have estimated the magnitude that the *V*-band Nickel data would have if it followed the same changes in brightness that the CSS data experienced between days 0 and 72. This results in a projected peak *V*-band magnitude of −19.14 in the Nickel data, which we use as the *V*-band peak estimate. Note, however, that SN 2014ab's peak magnitude occurs on the discovery date, with a gap of data in the 212 d prior, suggesting that we only have estimated a lower limit to the peak brightness of SN 2014ab.

The decline rate for SN 2014ab was ∼0.0034 mag d^{-1} in the CSS data and ∼0.0079 mag d^{-1} in the Nickel data, with the somewhat steeper decline in Nickel data reflecting the later dates that were sampled. We compare the light-curve decline rates to those of other SNe in Section 4.2.

3.3 SN location

We find astrometric fits to both the Nickel and Kuiper telescope images (Fig. 3) using astrometry.net (Lang et al. 2010). We then measure the location of the host galaxy from the Kuiper image and the location of the SN from the Nickel image after template subtraction using radial profile fits to a Moffat distribution (Moffat 1969). We determine the uncertainty in the location of the centroid by replicating the noise level in each image and refitting the centroid 100 times. The location of the SN is measured to be α(J2000) = $13^{\mathrm{h}}48^{\mathrm{m}}06\overset{\mathrm{s}}{.}05$ and δ(J2000) = $+07^\circ23'16\overset{''}{.}12 \pm 0.01''$, and the location of the host galaxy is measured to be α(J2000) = $13^{\mathrm{h}}48^{\mathrm{m}}06\overset{\mathrm{s}}{.}01$ and δ(J2000) = $+07^\circ23'15\overset{''}{.}41 \pm 0.3''$. The difference between these is $\Delta\alpha = 0.05^{\mathrm{s}} \pm 0.25^{\mathrm{s}}$ and $\Delta\delta = 0.71'' \pm 0.17''$. $\Delta\delta$ is bigger than the uncertainty in the $\Delta\delta$, suggesting that the SN is offset from the host-galaxy nucleus by roughly 0.71 arcsec. Given the distance to SN 2014ab of

Table 1. Spectroscopic observations of SN 2014ab.

Year-Month-Day	Day[a]	Telescope/Instrument	Wavelength range (Å)	$\sim R\,(\lambda/\Delta\lambda)$
2014-03-10	57	ESO-NTT/EFOSC2	3585–9065	350
2014-03-23	70	ESO-VLT/X-shooter	2923–24 241	3500
2014-03-24	71	Lick/Kast	3421–9775	600
2014-03-29	76	Bok/SPOL	3911–7373	200
2014-03-30	77	Bok/SPOL	3909–7375	200
2014-03-31	78	Bok/SPOL	3912–7375	200
2014-04-02	80	Bok/SPOL	3910–7377	200
2014-04-08	86	LCO/FLOYDS	4888–11 003	550
2014-04-09	87	LCO/FLOYDS	4892–9096	550
2014-04-11	89	LCO/FLOYDS	4886–9770	550
2014-04-20	98	LCO/FLOYDS	3960–7036	550
2014-04-20	98	MMT/SPOL	3910–9090	400
2014-04-23	101	LCO/FLOYDS	3913–9779	550
2014-04-24	102	ESO-VLT/X-shooter	2923–24 241	3500
2014-04-26	104	Kuiper/SPOL	3912–7375	200
2014-04-27	105	Kuiper/SPOL	3911–7372	200
2014-04-28	106	Kuiper/SPOL	3908–7375	200
2014-04-30	108	Lick/Kast	3420–10 261	600
2014-05-01	109	Kuiper/SPOL	3910–7377	200
2014-05-07	115	LCO/FLOYDS	3910–9774	550
2014-05-19	127	Magellan/IMACS	5477–7028	1600
2014-05-22	130	LCO/FLOYDS	3911–9776	550
2014-05-23	131	Bok/SPOL	3911–7379	200
2014-05-24	132	Bok/SPOL	3912–7375	200
2014-05-26	134	Bok/SPOL	3914–7379	200
2014-05-28	136	Lick/Kast	3421–9774	600
2014-06-21	160	Lick/Kast	3382–9970	600
2014-06-22	161	Kuiper/SPOL	3911–7379	200
2014-06-23	162	Kuiper/SPOL	3910–7376	200
2014-06-24	163	Kuiper/SPOL	3911–7375	200
2014-06-24	163	ESO-VLT/X-shooter	2923–24 239	3500
2014-06-26	165	Kuiper/SPOL	3909–7375	200
2014-06-29	168	ESO-VLT/X-shooter	2923–24 239	3500
2014-06-30	169	Lick/Kast	3373–10 266	600
2014-07-19	188	ESO-VLT/X-shooter	2923–24 239	3500
2018-04-14	1553	MMT/Bluechannel	5588–6863	3310

[a]Days since adopted discovery date (2014 January 12.4755 UT).

105.7 Mpc, it has a projected distance from the nucleus of the host galaxy of ∼364 pc. This indicates that SN 2014ab is not a nuclear transient like a TDE.

3.4 Spectral morphology

We detect a variety of spectral features in the 36 different spectra. Intermediate-width H α and H β emission are the most prominent spectral features present from day 57 to day 188. H β shows a broad, shallow, blueshifted absorption feature with a minimum of the absorption at $v \approx -8000\,\mathrm{km\,s^{-1}}$, and with the blue edge of the absorption extending to about $-17\,000\,\mathrm{km\,s^{-1}}$ (see Fig. 7). We do not see similarly strong, broad absorption in H α. H α and H β both exhibit narrow blueshifted absorption lines ($v \approx -80\,\mathrm{km\,s^{-1}}$; see Fig. 8) in the higher resolution spectra we obtained. The Ca II near-IR triplet (a blend of λ8498, λ8542, and λ8662) is strong in emission in SN 2014ab at all epochs that we observe, though there may be a contribution from O I λ8446 excited by Ly β fluorescence here, as suggested in Moriya et al. 2020. We also detect a number of weaker emission features in many of the optical spectra: these include H δ, H γ, and [O III] $\lambda\lambda$4959, 5007. Narrow H α emission is distinct from the intermediate-width feature in our higher resolution spectra, but it is blended with the intermediate-width component in our lower resolution spectra. X-shooter spectra extend into the near-IR (∼2.4 μm,), revealing a number of emission features. Most prominently, we detect He I λ10 830, Pa β, Br δ, and Br γ. We also detect weaker emission features of presumably Pa γ, O I λ11,287, Br 12-4, Br 11-4, Br 10-4, and He I λ20 589.

Many of the most prominent emission features (H α, H β, and Pa β) have intermediate-width emission components that remain constant with time throughout all of the spectra (see Fig. 9). These lines show asymmetric profiles with a net blueshift. The blueshifted emission component of these prominent lines is stronger than the redshifted component at all epochs. The intermediate-width H α emission reaches half maximum intensity at $\sim 2000\,\mathrm{km\,s^{-1}}$ on the blue side and $\sim 1000\,\mathrm{km\,s^{-1}}$ on the red side. This intermediate-width component extends out to ∼4500–6000 km s^{-1} on the blue side before reaching 10 per cent of maximum intensity and ∼4000–5000 km s^{-1} on the red side before reaching 10 per cent of maximum intensity. The centre of the intermediate-width component of H α is offset by $v \approx -500\,\mathrm{km\,s^{-1}}$, likely due to the CSM interaction approaching us obscuring the redshifted intermediate-width emission component. Overall, the spectra for SN 2014ab are very similar to those of SN 2010jl, including the blueshifted profile. However, the broad, blueshifted absorption seen in H β in SN 2014ab is stronger than in SN 2010jl (Smith et al. 2012).

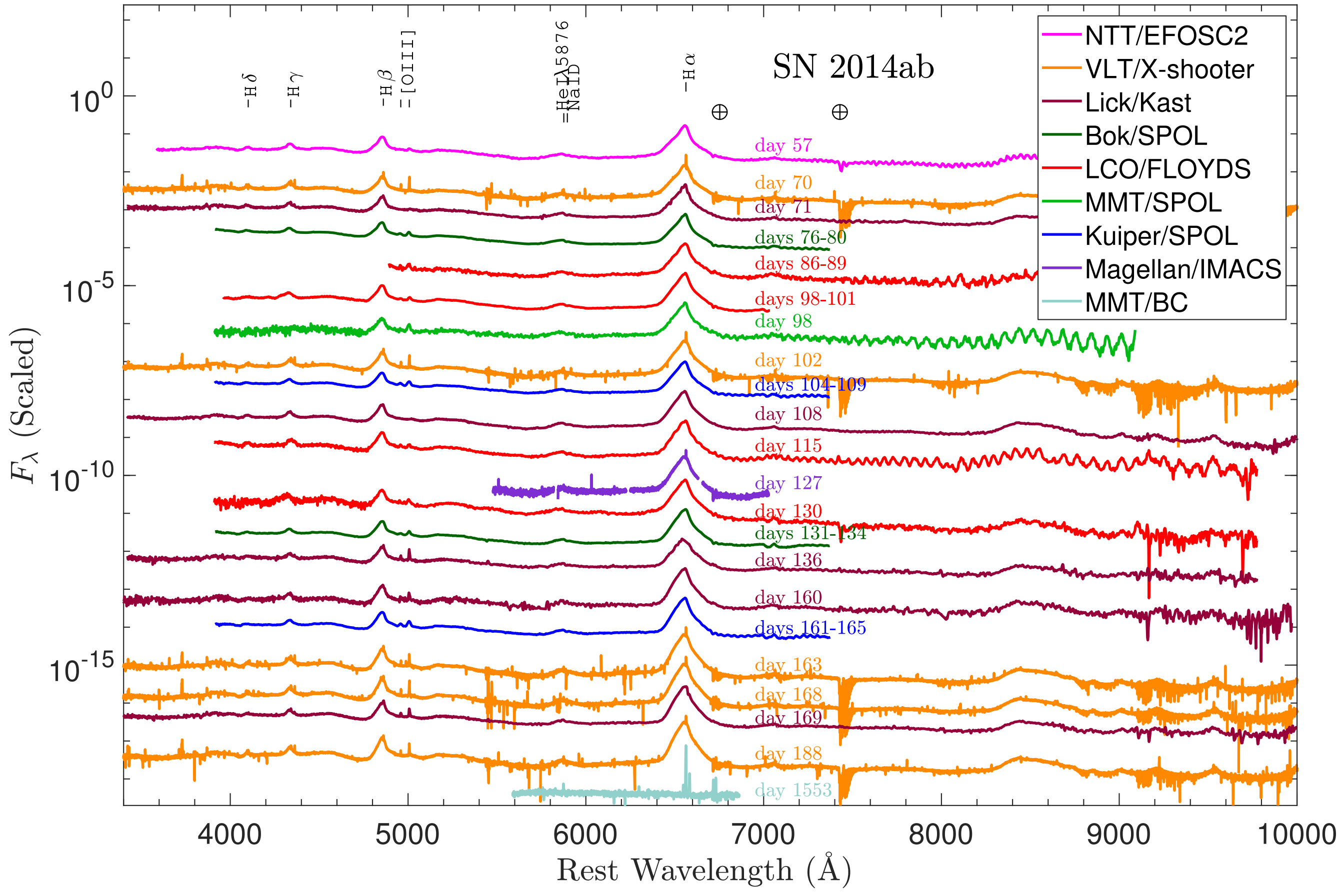

Figure 4. Visual-wavelength spectra of SN 2014ab. All spectra were corrected for reddening using $E_{B-V} = 0.083$ mag, which accounts for the total Milky Way and estimated host-galaxy reddening (see text). All spectra have also been corrected for host-galaxy redshift, and scaled for clarity (see Table 1). Additional small wavelength corrections were applied so that the narrow component of H α consistently matches the rest-frame wavelength of H α. Telluric features were not removed from some of the spectra and are marked with an Earth symbol; those longward of ∼9000 Å are not marked. Days since discovery date indicated.

3.5 Spectropolarimetry

Our spectropolarimetric analysis is performed primarily using the linear Stokes parameters, $q = Q/I$ and $u = U/I$, which are rotated 45° with respect to each other, allowing us to decompose the polarization signal into orthogonal components in position angle space. Typically, one can combine the Stokes parameters to obtain the polarization level, $P = \sqrt{Q^2 + U^2}$, and the position angle on the sky, $\theta = (1/2)\tan^{-1}(U/Q)$. However, since the definition of the polarization makes it a positive-definite value, it may seem artificially high in cases where we have a low signal-to-noise ratio because fluctuations will raise the mean polarization level significantly. To partially control for this effect, we also plot the rotated Stokes parameters, which are an attempt to rotate any significant non-zero polarization signal into *qRSP* while leaving noise in *uRSP*, though sharp changes in the *q*–*u* signal will remain in *uRSP* depending on the value of $\theta_{\rm smooth}$ that is used for rotation. We use the rotated Stokes parameters $qRSP = q\cos(2\theta_{\rm smooth}) + u\sin(2\theta_{\rm smooth})$ and $uRSP = -q\sin(2\theta_{\rm smooth}) + u\cos(2\theta_{\rm smooth})$, and the optimal polarization, $P_{\rm opt} = P - \sigma_P^2/P$ (Wang, Wheeler & Höflich 1997). The $\theta_{\rm smooth}$ value we use is a moving average over 100 Å, so changes in the polarization signal that occur alongside changes in the polarization angle within a small wavelength range will not be effectively rotated into *qRSP*.

We measure the optimal polarization over two wavelength ranges that are meant to avoid spectral lines in order to obtain the best measurement of the continuum polarization. In particular, we measure the optimal polarization at 5100–5700 Å and 6000–6300 Å for each of our epochs of spectropolarimetry. These values range between 0.07 per cent ± 0.04 per cent and 0.43 per cent ± 0.09 per cent (shown in Tables 2 and 3), studied in detail in Fig. 10, and are also shown in Figs 11–13. Uncertainty values on *q* and *u* were determined from the root-mean-square (rms) noise in the measured *q* and *u* spectra, which does not include systematic errors. These uncertainties were then propagated to the uncertainty on the integrated *q*, integrated *u*, and optimal polarization estimates. Although debiased, the optimal polarization level is still not a perfect measure, so we attempt to perform our analysis in the *Q* and *U* plane whenever possible. This allows us to avoid problems with the positive-definite nature of polarization.

We must address the tricky issue of ISP in order to determine what level of polarization signal is actually coming from our target of interest. It is difficult to measure the combined level of the ISP coming from the Milky Way and from the host galaxy of the SN. Fortunately, however, Na I D absorption lines in our spectra provide constraints on the total reddening along our line of sight. This allows us to predict very low ISP values for SN 2014ab.

In Section 3.1, we found a low value for the reddening of $E_{B-V} = 0.083$ mag based on Na I D absorption plus Milky Way reddening. We adopt this total extinction level when dereddening our spectra in Fig. 4 and all subsequent analysis. Additionally, the ISP–reddening

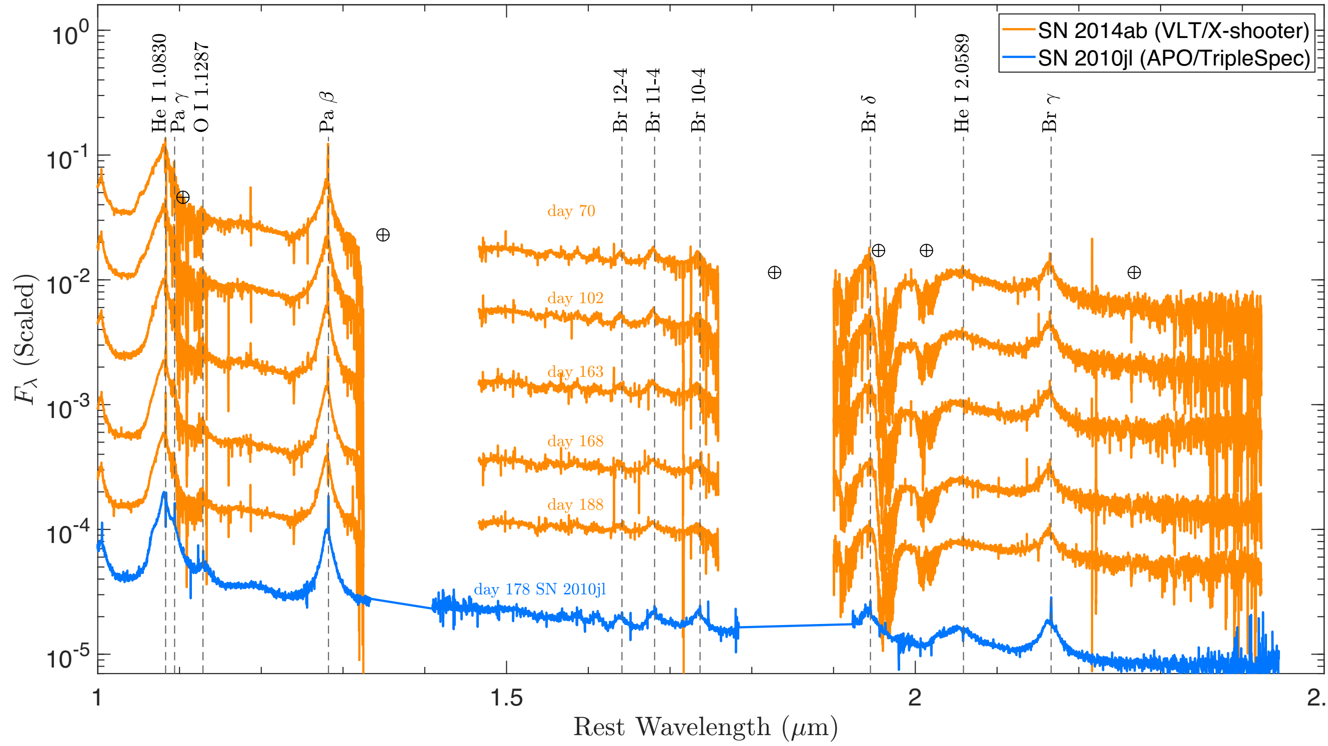

Figure 5. Near-IR spectra of SN 2014ab. All spectra were corrected for reddening using $E_{B-V} = 0.083$ mag, which accounts for the total Milky Way and estimated host-galaxy reddening (see text). All spectra have also been corrected for host-galaxy redshift, and scaled for clarity (see Table 1). Additional small wavelength corrections were applied so that the narrow component of H α consistently matches the rest-frame wavelength of H α, though H α is not shown in this figure. Telluric features were not removed and are marked with an Earth symbol. We also plot a spectrum of SN 2010jl 178 d after earliest detection for comparison (Borish et al. 2015).

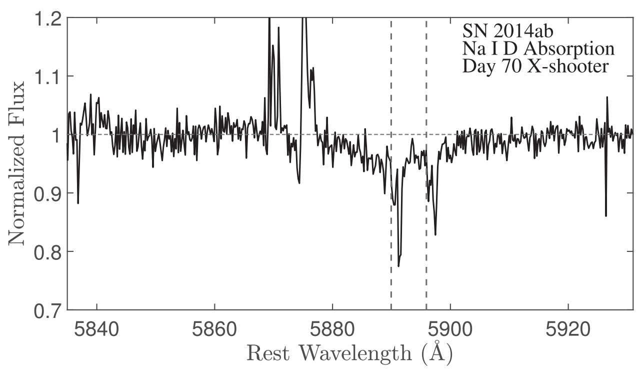

Figure 6. An $R = 3500$ X-shooter spectrum taken on day 70 showing the sodium doublet absorption that we use to constrain the host-galaxy extinction and interstellar polarization (ISP). The spectrum has been redshift corrected using the average redshift of the host galaxy and then aligned to the narrow component of H α emission. Vertical dashed lines show the rest-frame wavelengths of the Na I D lines. The observed Na I D absorption lines are offset slightly ($\sim$54 km s^{-1}) from their rest wavelengths because of host-galaxy rotation.

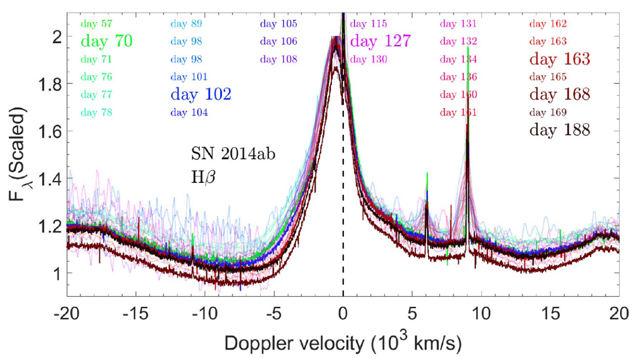

Figure 7. The progression of the H β line over the course of the $\sim$150 d during which we obtained spectra. Medium- and high-resolution spectra are shown fully opaque and have their dates labelled with larger text. Because the spectra overlap heavily owing to a lack of change in the line profile, low-resolution spectra are shown transparently and have small date labels. A broad, shallow P-Cygni absorption feature is seen, likely arising in the SN ejecta. This absorption feature has a minimum at $v \approx -8000$ km s^{-1}, and a blue edge out to $v \approx -18\,000$ km s^{-1}.

relation from Serkowski, Mathewson & Ford (1975) suggests that ISP $<9E_{B-V}$ per cent for Milky Way dust, which means that we can use the measure of E_{B-V} from the Na I D absorption lines and the Milky Way to place a constraint on the level of the ISP to <0.75 per cent. In doing so, we have applied the relation from Serkowski et al. (1975) to the dust in the host galaxy as well as the Milky Way, though this is not a perfect assumption (Leonard et al. 2000; Porter et al. 2016). We are not able to constrain the likely location of the total ISP in the q–u plane, so we do not subtract the ISP directly from our measurements. If the full extent of the ISP were aligned exactly opposite in the q–u plane to our strongest continuum polarization signal measurement for SN 2014ab (0.43 per cent $\pm$ 0.04 per cent), then SN 2014ab would have a continuum polarization and line polarization of 1.18 per cent. We use this as a conservative upper limit on the continuum and line polarization for SN 2014ab. This is lower than that for other

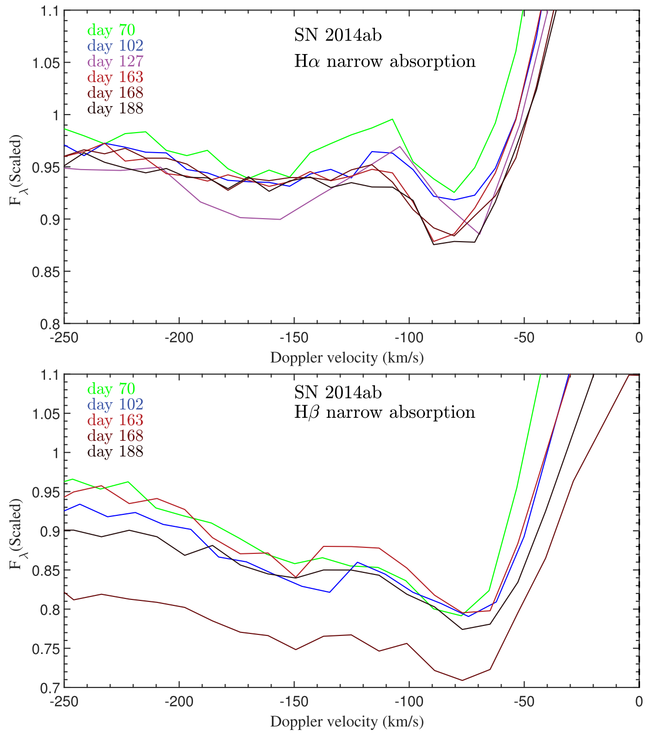

Figure 8. *Top panel:* Narrow absorption features of H α ($v \approx -80\,\mathrm{km\,s^{-1}}$) are seen in all of our higher resolution spectra. *Bottom panel:* The same for H β.

SNe IIn with published spectropolarimetry (SN 1997eg: Hoffman et al. 2008; SN 1998S: Leonard et al. 2000; SN 2006tf: Smith et al. 2008; SN 2009ip: Mauerhan et al. 2014; Reilly et al. 2017; SN 2012ab: Bilinski et al. 2018) and is discussed in more detail Section 4.6.

Figs 11–13 show the spectropolarimetric data plotted in the *q*–*u* plane. The polarization signal is weak at every one of our five epochs spanning from day 76 to day 165, although the signal becomes much noisier by our later epochs. The *q* and *u* values are relatively evenly scattered around the origin in every epoch, though we see a slight shift in the optimal polarization value across the continuum between the first epoch of spectropolarimetry and the remaining four epochs. Fig. 10 shows the *q* and *u* values integrated across two wide continuum regions (5100–5700 Å and 6100–6400 Å). The error bars are likely an underestimate of the true uncertainty, so we conclude that only the shift in polarization from the first epoch to the later epochs is statistically significant and consistent across both continuum wavelength regions.

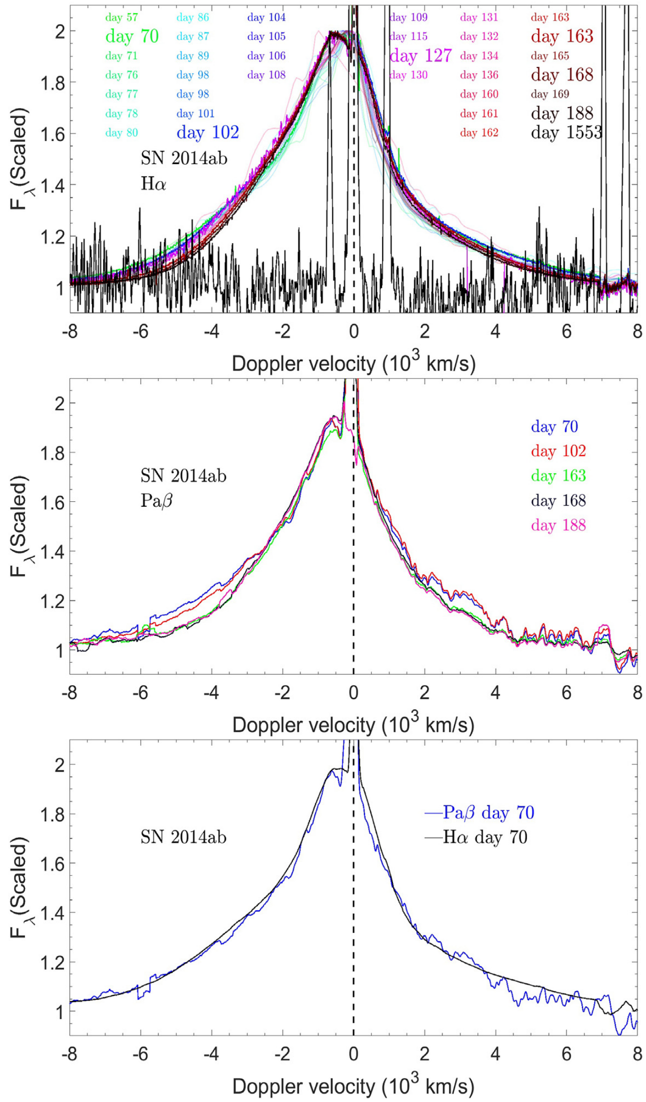

Figure 9. *Top panel:* The progression of the H α line over the course of the ~150 d during which we obtained spectra. Medium- and high-resolution spectra are shown fully opaque and have their dates labelled with larger text. Because the spectra overlap heavily owing to a lack of change in the line profile, low-resolution spectra are shown transparently and have small date labels. *Middle panel:* The progression of the Pa β line over the course of the ~70 d during which we obtained near-IR spectra. *Bottom panel:* A comparison of the first Pa β line and its H α counterpart. See Section 4.5 for a discussion of the asymmetric H α and Pa β emission line profiles.

Table 2. Continuum polarization measurements across 5100–5700 Å.

Epoch (days)	P_{opt} (%)	Integrated *q* (%)	Integrated *u* (%)
76–80	0.10 ± 0.03	0.10 ± 0.03	0.05 ± 0.03
98	0.24 ± 0.03	− 0.20 ± 0.03	0.14 ± 0.03
104–109	0.30 ± 0.07	− 0.23 ± 0.07	0.21 ± 0.07
131–134	0.31 ± 0.05	− 0.21 ± 0.05	0.25 ± 0.05
161–165	0.32 ± 0.09	− 0.099 ± 0.09	0.34 ± 0.09

4 DISCUSSION

4.1 SN, AGN, or TDE

Because SN 2014ab is within 1 arcsec of its host-galaxy centre, we consider the possibility that it is an active galactic nucleus (AGN) or TDE. The light curve of SN 2014ab (see Section 3.2) shows a relatively smooth drop of ~1 mag over the course of ~150 d. During this period of time, the equivalent width of the H α line increases roughly twofold (see Fig. 14), probably caused by a fading continuum paired with a persistent bright CSM interaction region. While AGNs can exhibit such variations on this time-scale (Ulrich, Maraschi & Urry 1997), they do not generally brighten and fade only once over

Table 3. Continuum polarization measurements across 6100–6300 Å.

Epoch (days)	$P_{\rm opt}$ (%)	Integrated q (%)	Integrated u (%)
76–80	0.07 ± 0.04	0.08 ± 0.04	0.04 ± 0.04
98	0.21 ± 0.04	− 0.17 ± 0.04	0.14 ± 0.04
104–109	0.43 ± 0.09	0.02 ± 0.10	0.44 ± 0.09
131–134	0.36 ± 0.08	− 0.11 ± 0.07	0.36 ± 0.08
161–165	0.38 ± 0.12	− 0.41 ± 0.12	0.02 ± 0.12

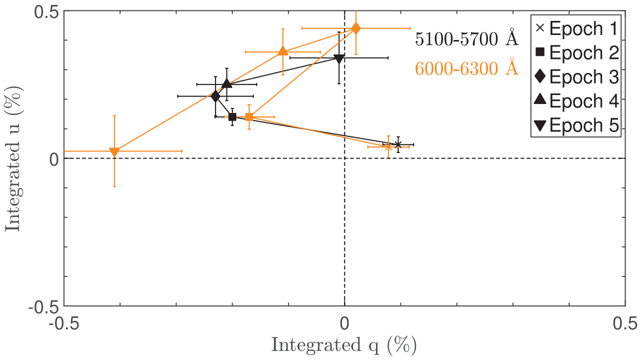

Figure 10. The integrated continuum q and u values for the five different epochs of spectropolarimetry. Error bars are estimated from the statistical rms noise and do not include systematic errors, so they are likely an underestimate of the true uncertainty. A slight change of around 0.2–0.3 per cent in the intrinsic polarization of SN 2014ab is confidently shown only between epoch 1 and epochs 2–5.

the course of a ∼11 yr time-scale. Additionally, AGNs tend to have a number of forbidden emission lines that we do not detect. These include [O I] λλ6300, 6364, [O III] λλ4959, 5007, [N I] λ5199, and [N II] λλ6548, 6583. The He II λ4686 line is often quite strong compared to the Balmer series in AGNs, but we do not detect it in our spectra. The late-time spectrum of SN 2014ab taken on day 1553 shows only narrow H α emission, whereas the intermediate-width component is completely gone. For these reasons, we find it unlikely that SN 2014ab is an AGN.

We also consider the possibility that SN 2014ab may be a TDE because TDEs also produce bright asymmetric signatures and are found coincident with the central region of their host galaxy. Unlike an AGN, a TDE is consistent with the long stable CSS photometry for years prior to the brightening event, followed by a decrease in brightness that does not rebrighten again. Since the explosion date of SN 2014ab could be anywhere from day −212 to day 0, it is difficult to compare our light curve to the theoretical decline rate in TDEs ($t^{-5/3}$; Rees 1988; Evans & Kochanek 1989; Phinney 1989). However, none of the TDE light curves based on all possible explosion dates match that of our observed light curve and we show the best case TDE decline curve (which assumes an explosion date of day −212) in Fig. 3. Our light curve shows a steepening in the decline of SN 2014ab and a duration of over 150 d, which is uncharacteristic of TDEs. If the event we observed was in fact a TDE, we would expect the light curve to become gradually flatter. Spectroscopically, we would expect there to be an offset between the narrow lines and the intermediate-width lines in the case of a TDE, which we do see (Strubbe & Quataert 2009). However, we do not detect any strong He II emission, which is thought to be common in TDEs, though not always detected (Gezari et al. 2012; Arcavi et al. 2014). Overall, the shape of the light curve, the long duration of the event, and the lack of He II emission suggest that SN 2014ab is not a TDE. Henceforth, we assume that SN 2014ab is a core-collapse SN with strong CSM interaction.

4.2 Light curve

SN 2014ab is a luminous example among SNe IIn. Its projected peak in the Nickel photometry was at $M_V = -19.14$ mag, approaching values of superluminous SNe, and it remained bright, declining slowly over the next 211 d to a brightness of −17.89 mag (see Section 3.2 for a summary of the photometric data).

The sustained high luminosity suggests that SN 2014ab is more akin to superluminous SNe IIn like SN 2010jl (Patat et al. 2011) and SN 2006tf (Smith et al. 2008), albeit with a slightly lower peak luminosity, and quite different from faster declining SNe IIn like SN 1998S (Fassia et al. 2000). Of course, the true peak luminosity of SN 2014ab may have been higher than its observed peak because of its relatively late discovery. Fig. 15 shows a comparison of several SN light curves. Although some SNe IIn (such as SN 1998S) exhibit light-curve decline rates similar to those of SNe II-L (such as SN 2003hf), other SNe IIn (such as SN 2014ab and SN 2010jl) exhibit slower light-curve decline rates for much longer durations. We attribute the extended and bright plateau in SN 2014ab to strong CSM interaction.

4.3 Lack of spectral evolution

Although SN 2014ab drops in brightness significantly over the course of the ∼150 d during which we also have spectra, the spectra show little qualitative change. This suggests that we did not observe SN 2014ab during its early stages, as most SNe IIn are observed to have drastically changing early-time spectra as they transition from optically thick CSM and electron scattering line profiles to later times when emission from the cold dense shell is revealed (Smith 2017). Instead, we are likely observing SN 2014ab while the SN ejecta are crashing into increasingly distant but smoothly distributed CSM, creating spectral features that are similar at each epoch because the advancing shock speed and CSM density change slowly. Some SNe IIn (such as SN 2010jl) have also shown spectral evolution due to dust formation as early as 30 d after explosion (Smith et al. 2012), though we do not see this evolution in SN 2014ab.

4.4 CSM interaction luminosity

The strong intermediate-width H α component seen in our spectra and the spectral similarity to SN 2010jl suggest that CSM interaction dominates the emitted radiation in SN 2014ab. If the CSM interaction is powering most of the luminosity, then we can estimate a lower limit to the wind-density parameter ($w = \dot{M}_{\rm CSM}/v_{\rm w}$, where $v_{\rm w}$ is the velocity of the pre-shock wind) prior to the explosion of SN 2014ab. We calculate the wind-density parameter as

$$w = 2L/v_{\rm SN}^3, \tag{1}$$

where L is the observed luminosity and $v_{\rm SN}$ is the velocity of the post-shock shell (Smith et al. 2008).

This assumes instantaneous and 100 per cent efficient conversion of shock kinetic energy into radiation as well as spherical symmetry. In the case of less than 100 per cent efficient conversion or asymmetric clumping, a higher wind-density parameter would be required, resulting in a higher required mass-loss rate. The velocity of the post-shock shell is determined from the intermediate-width component of the H α line, which is measured to have a half width at half-maximum intensity of ∼2000 km s^{-1}. Although our R-band

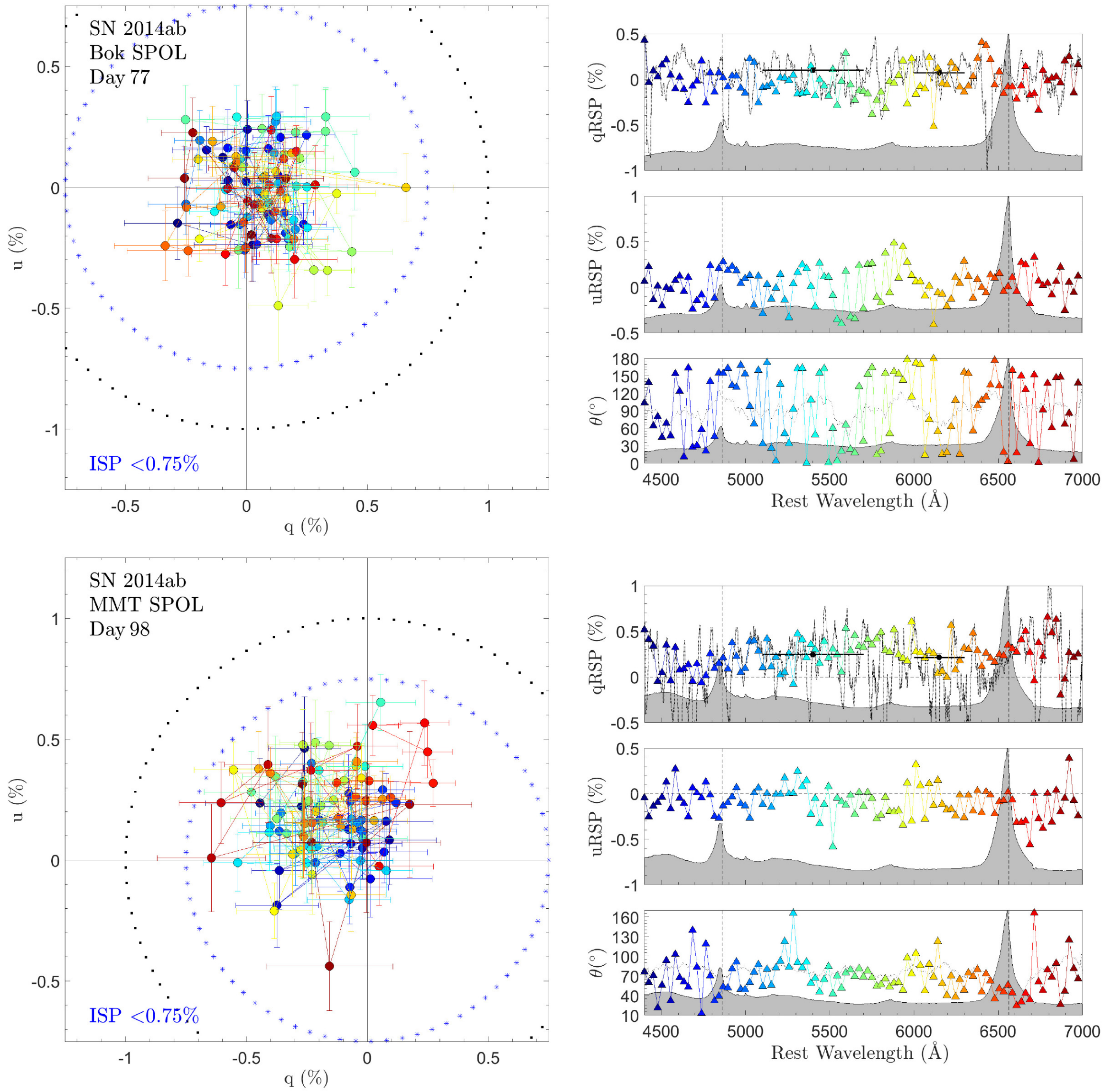

Figure 11. *Top panels:* *q–u* Stokes parameters, *qRSP–uRSP* rotated Stokes parameters, and position angle θ for SN 2014ab from the 90-inch Bok telescope on days 76–80 (data from multiple days combined). The dotted black line in the *qRSP* plot indicates the smoothed optimal polarization value. The dotted black line in the position-angle plot indicates the smoothed position angle, $\theta_{\rm smooth}$. The solid black point in the *qRSP* plot is the optimal polarization value measured across the continuum region designated by the horizontal black bars. The data are grouped into ~28 Å bins. Shaded regions show a scaled version of the total-flux spectrum. Vertical dashed lines are present at the wavelengths of H α and H β. Horizontal dashed lines are present at 0 in the *qRSP* and *uRSP* plots for clarity. We have adopted an ISP value of < 0.75 per cent (shown as a circle of blue asterisks) based on Na I D absorption-line measurements (see Section 3.5). Black dotted circles in the *q–u* plot indicate 1–2 per cent polarization. Colours, bins, and error bars in the *q–u* plots on the left correspond to those on the right, with wavelengths labelled on the right. *Bottom panels:* The same for the MMT data from day 98.

measurements do not extend to day 0, we assume a rough average $M_R \approx -19$ mag over the course of 200 d, and conservatively adopt no bolometric correction, to roughly estimate the average luminosity ($L \approx 3.1 \times 10^9$ L$_\odot$). We obtain a conservative estimate of the wind-density parameter of $\sim 3 \times 10^{18}$ g cm^{-1}. If we assume a steady wind velocity of $\sim$80 km s^{-1} (estimated from the P-Cygni absorption in H α) from the progenitor, we can estimate the mass-loss rate to be at least $\dot{M} \approx$ M$_\odot$ yr^{-1}($v_{\rm w}$/(80 km s^{-1})). This mass-loss rate is higher than any normal steady wind mass-loss, but is achievable by episodic super-Eddington winds of massive stars (Smith & Owocki 2006). The intermediate-width component of H α persists for over 150 d (and is likely a significant source of the luminosity of SN 2014ab going back another 50 d), so we can estimate the duration of its pre-SN mass-loss episode by determining how long pre-SN mass-loss must have been occurring. In order for the $\sim$2000 km s^{-1} shell to be continually running into CSM that was ejected at roughly 80 km s^{-1} for 200 d, the pre-SN mass-loss must have begun at least $T\, v_{\rm SN}/v_{\rm w} = 14$ yr before explosion, where T is the duration of the strong intermediate-width component of H α. This suggests a total mass-loss of ~ 5 M$_\odot$ in the 14 yr prior to explosion, comparable to the CSM mass inferred for some of the most luminous SNe IIn (Smith et al. 2007; Smith & McCray 2007; Ofek et al. 2014).

The variety of progenitor candidates for SNe IIn have widely differing mass-loss rates. Smith (2014) estimated that eruptive lumi-

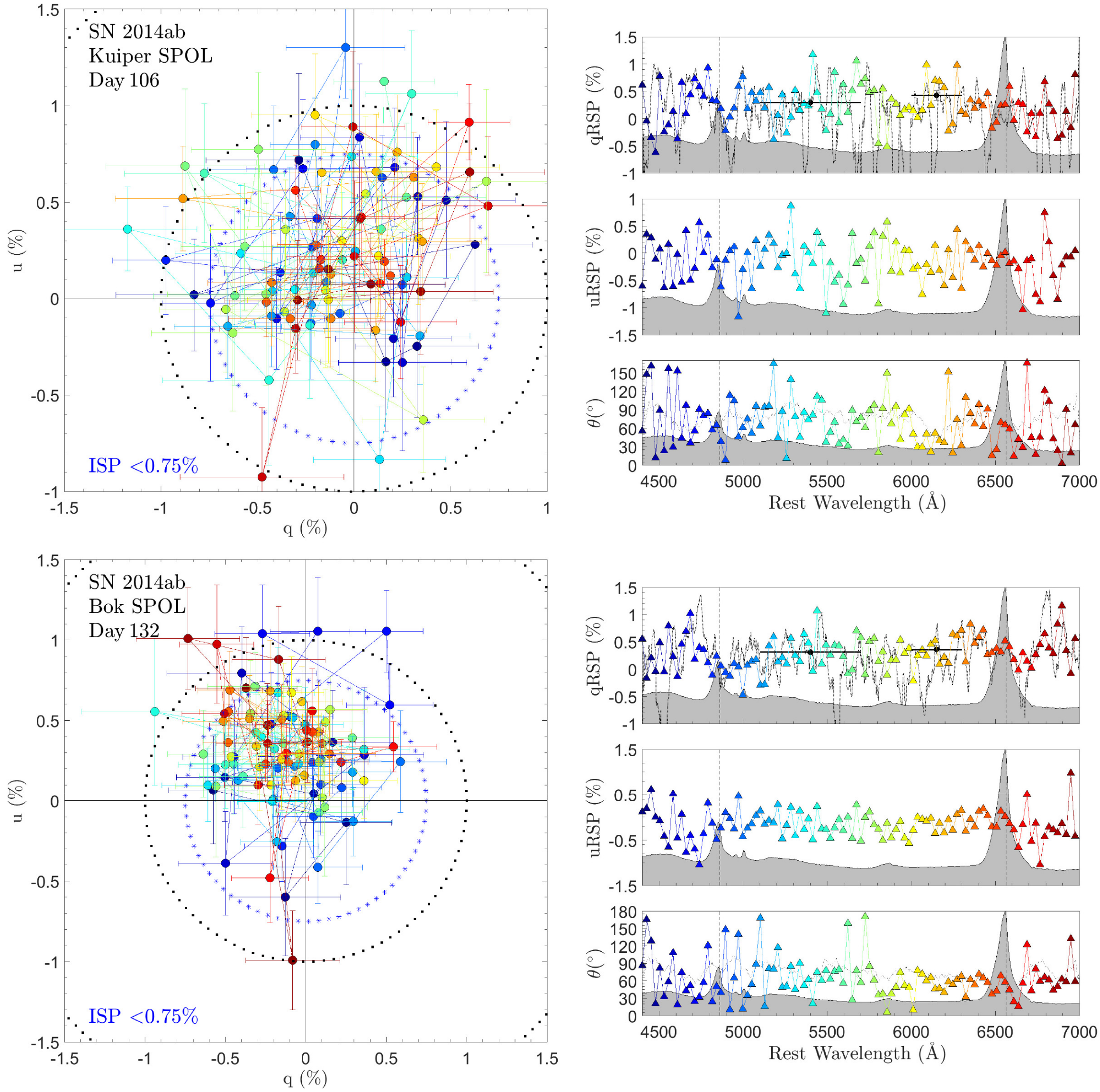

Figure 12. *Top panels:* The same as Fig. 11, but for Kuiper data from days 104 to 106. *Bottom panels:* The same for the 2.3-m Bok telescope data from days 131–134.

nous blue variable (LBV) progenitors can have mass-loss rates in the range of 0.01–10 $M_{\odot}$ yr^{-1}, while even very massive red supergiant or yellow hypergiant progenitors have mass-loss rates in the range of 10^{-4}–10^{-3} $M_{\odot}$ yr^{-1}. LBVs undergoing eruption are therefore the only known class of progenitors to SNe IIn that have mass-loss rates as high as those we measure for SN 2014ab (Smith & Owocki 2006; Smith 2014). The physical cause of this eruptive mass-loss remains unknown, but several ideas have been proposed, including wave-driven mass-loss during Ne, O, or Si burning (Quataert & Shiode 2012), pulsational pair eruptions (Woosley 2017) or other nuclear burning instabilities (Smith & Arnett 2014), and various types of binary interaction (Chevalier 2012; Smith & Arnett 2014).

4.5 Asymmetric H α and Pa β

Fig. 9 shows the H α and Pa β emission-line profiles, scaled to the continuum fit beyond the wings of each line. As the red wing of Pa β is blurred with telluric features, this continuum estimate contains greater uncertainty not reflected in the line-strength measurements shown in Fig. 16. The blueshifted side of both lines is clearly stronger than the redshifted side of the line at all epochs. The early-time spectra for both emission lines are slightly wider on the blueshifted side of the line than in the late-time spectra. The H α emission line in the day 57 spectrum has a width on the blueshifted side at 10 per cent of maximum intensity of $\sim$6000 km s^{-1}, whereas the day 188 spectrum has a width on the blueshifted side at 10 per cent of maximum intensity of $\sim$4500 km s^{-1}. Emission in the wings of the line likely arises in the SN ejecta, with slower SN ejecta hitting the shock front as time progresses. It is possible that we are not seeing this same effect on the redshifted side of the emission line because it is obscured by the blueshifted CSM interaction region (see Section 4.8 and Fig. 19 for a more detailed discussion of the line of sight).

We measure the flux of the H α line above the continuum level on the redshifted and blueshifted sides of the line separately ($v = 0$ is

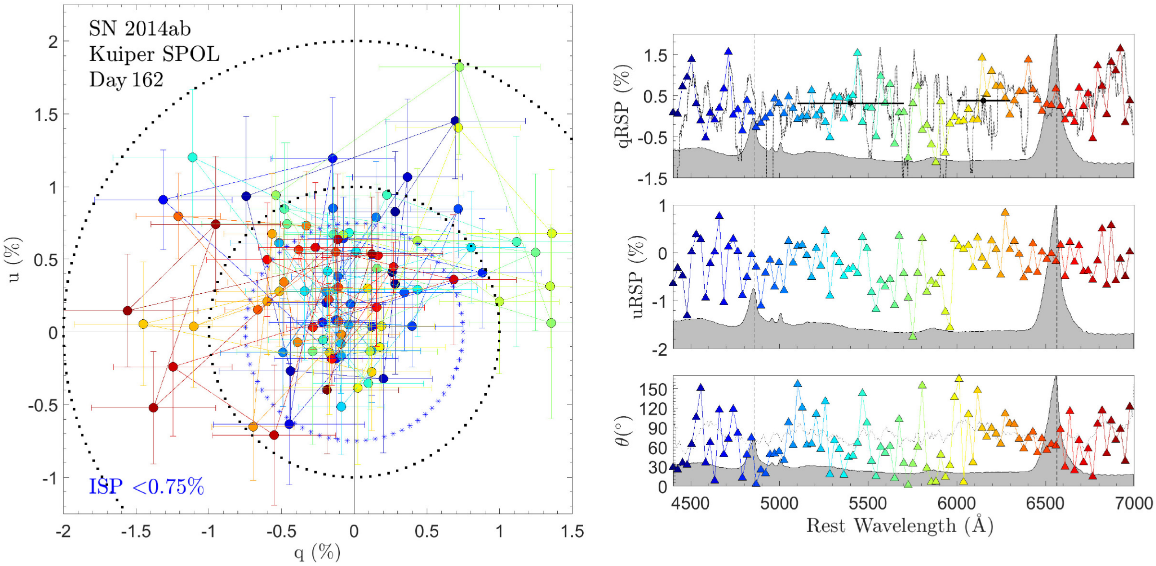

Figure 13. The same as Fig. 11, but for Kuiper data from days 161 to 165.

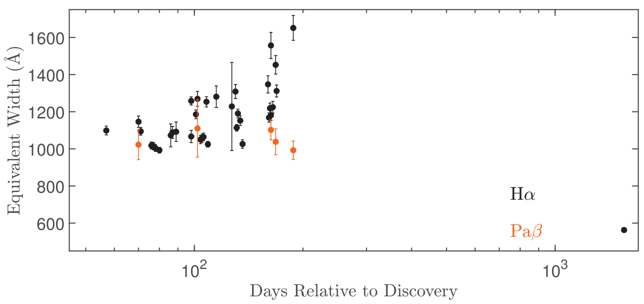

Figure 14. The equivalent width of H α (black) and Pa β (orange) at all epochs. As the light curve of SN 2014ab fades ~1 mag over the course of ~150 d (so that the visual continuum fades by a factor of 2–2.5), the equivalent width of H α increases by a factor of ~ 1.5.

chosen to align with the narrow component in high-resolution spectra and where we would expect the narrow component in low-resolution spectra based on temporal interpolation between the high-resolution spectra). The blue/red ratio of these fluxes is shown in Fig. 16. Throughout all epochs, we find that the blueshifted component of the H α line is roughly 1.4 times as strong as the redshifted component. This may in principle be due to dust formation, occultation by the SN ejecta or CSM interaction region, electron scattering, or real geometrical asymmetries. Since the SN was first observed during the decline phase in its light curve and the spectra remain surprisingly similar throughout all epochs even as the SN fades, we find it unlikely that the SN ejecta are still optically thick in the continuum at late times. If the SN ejecta were optically thick initially, then over the course of the 150 d during which we obtain spectra, we would have expected the redshifted component of the spectra to become relatively stronger as the SN ejecta become less optically thick.

In order to probe whether dust formation is likely, we also perform the same blueshifted versus redshifted component measurement on the Pa β line, though our estimates of the redshifted flux are prone to noise from atmospheric absorption. The blue/red ratio of fluxes for Pa β is shown in Fig. 16. Dust extinction by small grains is wavelength dependent as was found in SN 2010jl (Smith et al. 2012), but we do not see a wavelength-dependent asymmetry in the lines of H α and Pa β in SN 2014ab. Instead, we see a similar 1.4:1 strength in the blueshifted component compared to the redshifted component for both H α and Pa β. Lastly, electron scattering has been shown to produce augmented blueshifted emission profiles that are offset from the rest frame given high velocities (Dessart et al. 2009). However, the H α and Pa β emission-line profiles we observe have wider blue wings than red wings (see Fig. 17), unlike those seen in high-velocity electron scattering profiles. We also do not observe strong blueshifted absorption that is suggested in the case of electron scattering. This implies that occultation by the optically thick CSM interaction region, extinction from very large dust grains, or real geometrical asymmetries in the SN ejecta or CSM are the cause of these asymmetric line profiles.

4.6 Weak symmetry in the face-on viewing plane

We estimate a low value for the ISP (< 0.75 per cent) based on low Na I D equivalent widths and the relation between these equivalent widths and reddening provided by Poznanski et al. (2012). The q and u values for the first four epochs of spectropolarimetry fall mostly within the constraint on the ISP (see Figs 11 and 12). The q and u values for the last epoch of spectropolarimetry extend to about twice the estimate of the ISP and have much larger error bars, but still average a polarization measurement below that of the ISP constraint (see Fig. 13). Fig. 10 shows a slight change in the integrated q and u values between the first epoch and the last four epochs of spectropolarimetry. This is also seen by the slight increase in the optimal polarization measured in the continuum shown in Tables 2 and 3. The change in the continuum polarization cannot be caused by the relatively constant ISP, and therefore we conclude that there is a slight change (0.36 per cent) in the intrinsic polarization of SN 2014ab. This slight change sets a lower limit to the intrinsic polarization to SN 2014ab of at least 0.36 per cent, which when combined with our upper limit of 1.18 per cent discussed in Section 3.5 suggests that SN 2014ab has low continuum polarization compared to other SNe IIn with published spectropolarimetry. Thus, despite the asymmetries measured in the emission lines of SN 2014ab, spectropolarimetry at five different epochs (spanning from day 76 to day 165) suggests that the face-on viewing plane

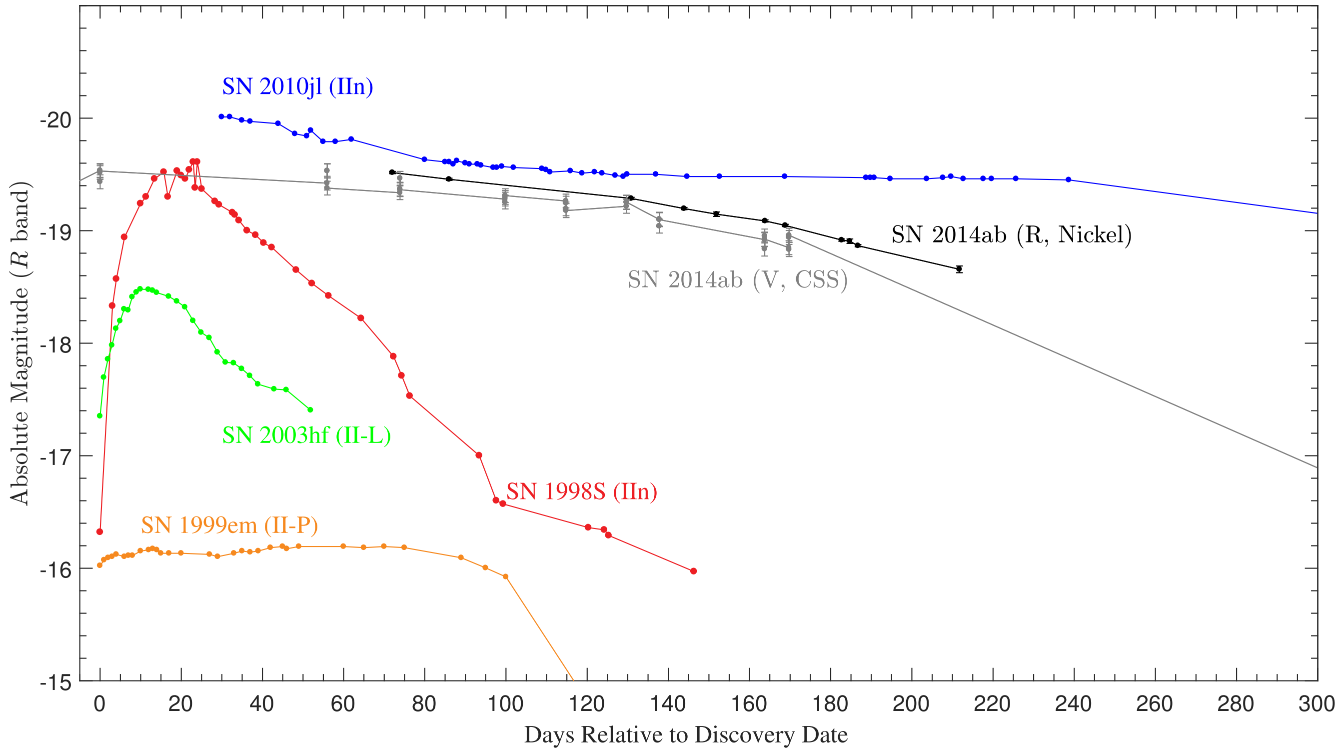

Figure 15. *R*-band (Nickel telescope) and *V*-band (CSS, host galaxy subtracted) observations of SN 2014ab relative to the discovery date of 2014 January 12.4755. For comparison, we have included the *R*-band light curves of the Type II-P SN 1999em (orange; Leonard et al. 2002b), the Type II-L SN 2003hf (green; Faran et al. 2014a), the Type IIn SN 1998S (red; Fassia et al. 2000; Poon et al. 2011), and the Type IIn SN 2010jl (blue; Williams, private communication).

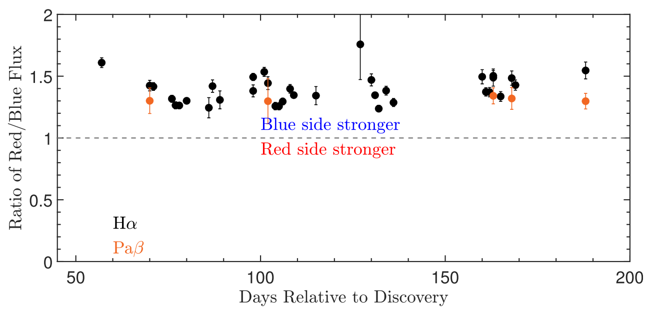

Figure 16. Ratio of the flux for the blueshifted side of a line compared to the redshifted side of a line, for H α (black) and Pa β (orange). This gives a quantitative indication of the relative asymmetry in the line profile. Note that the statistical errors shown for Pa β are likely an underestimate of the true error because the continuum level on the redshifted side of the line is extremely uncertain owing to blending with telluric absorption.

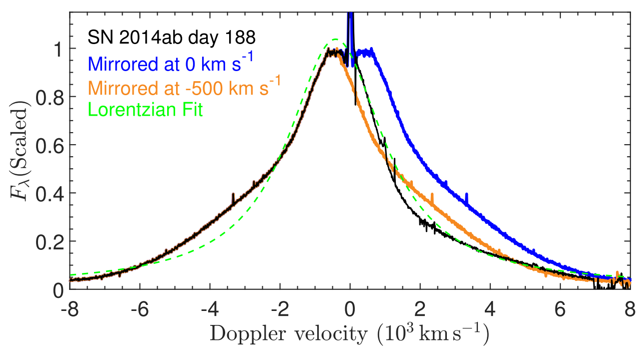

Figure 17. The day 188 ESO-VLT X-shooter spectrum of H α is shown in black. The blueshifted wing of the line has also been mirrored across a vertical line at 0 km s^{-1} (blue) and at -500 km s^{-1} (orange). A best-fitting Lorentzian is overplotted as a dashed green line. A Gaussian, Lorentzian, and Voigt profile all fail to fit the asymmetric wings of the H α emission-line profile.

has much less deviation from circular symmetry compared to other SNe IIn.

4.7 Comparison to SN 2010jl

SN 2014ab shows many similarities to SN 2010jl, particularly in its near-IR spectra. Near-IR spectra of both SN 2014ab and SN 2010jl are plotted in Fig. 5 for comparison. The major features (He I λ10 830, Pa β, Br δ, and Br γ) are all very similar in both objects. Of particular interest is the fact that both Pa β lines have augmented intermediate-width blueshifted emission offset from the centre of the narrow Pa β emission component. Unlike SN 2014ab, SN 2010jl was observed to have a symmetric line profile for H α at early times (days 29 and 59; Smith et al. 2012; Fransson et al. 2014), which then evolved to the blueshifted profile similar to SN 2014ab by day 85. Of course, SN 2014ab may have also had symmetric lines in its early evolution, since it seems to have been discovered relatively late. At late times (day 448 onward; Fransson et al. 2014), SN 2010jl is seen to be dominated by thermal emission from dust. When comparing the H α emission-line profile to that of Pa β, Smith et al. (2012) found that the blueshifted dominance is more pronounced at shorter wavelengths, likely because of the presence of dust. SN 2010jl has been suggested to have pre-existing dust (Andrews et al. 2011), post-shock dust formation (Smith et al. 2012; Maeda et al. 2013; Gall et al. 2014), or no dust (Zhang et al. 2012; Fransson et al. 2014), but SN 2014ab does not show a more pronounced blueshifted component at shorter wavelengths, implying that the asymmetry we observe is not caused by small grain dust.

Spectropolarimetry of SN 2010jl indicates continuum polarization as high as $\sim$2 per cent (Patat et al. 2011; Williams et al., in preparation). Additionally, depolarization of H α and H β suggests that this continuum polarization reflects real asymmetries in the SN 2010jl photosphere. Based on models with an axially symmetric prolate morphology, Dessart, Audit & Hillier (2015) find a pole-to-equator density ratio of $\sim$2.6. On the other hand, SN 2014ab was observed to have very low continuum polarization at five epochs, and exhibits no sign of depolarization near H α.

Another key difference between SN 2014ab and SN 2010jl is the prominence of their H β absorption lines and Ca II near-IR triplet emission lines, shown in Fig. 18. SN 2014ab shows stronger absorption in H β (as well as stronger broad absorption in H α and He I λ5876 and λ7065) and stronger emission in the Ca II near-IR triplet emission lines. This suggests that the light from the SN photosphere that we are seeing from SN 2014ab passes through a larger amount of SN ejecta than that of SN 2010jl.

4.8 Physical picture for SN 2014ab

SN 2014ab is a peculiar, luminous SN IIn. It is puzzling in the sense that it does not show strong evidence for asymmetry in its low level of polarization, but asymmetry is evident from the line profiles in the spectra. The large number of similarities between SN 2014ab and SN 2010jl provide motivation to consider a similar physical scenario for the two events, but certain key differences (polarization, broad P-Cygni absorption features) suggest that we may be looking at analogous events from different viewing angles.

The key features of SN 2014ab are interpreted in Fig. 19. We suggest that the majority of its luminosity likely arises in an equatorially concentrated or bipolar CSM interaction region, which wraps around the densest equatorial CSM. The continuum photosphere resides in this CSM interaction region and may therefore create a stronger blueshifted intermediate-width emission component if the continuum photosphere occults the redshifted side of the equatorial CSM interaction region. This CSM interaction region is likely formed from mass lost from the progenitor of SN 2014ab within the 10–20 yr prior to its death. The SN ejecta from the explosion itself are likely optically thin at the time of our observations and have faded, but their presence can be seen in the broad components of hydrogen Balmer emission lines, Ca II near-IR triplet emission lines, and broad H β absorption.

The narrow blueshifted H α and H β absorption as well as the narrow H α emission persist throughout the evolution, so they likely arise from distant CSM along our line of sight that has not yet been overrun. These features place the likely viewing angle for SN 2014ab along the axis of symmetry (i.e. above the pole), as labelled in Fig. 19, whereas SN 2010jl is probably observed from a different viewpoint shown in the schematic. From the viewpoint of SN 2014ab, spectropolarimetric data could imply a roughly circularly symmetric photosphere because we are seeing a disc or torus face-on, whereas from the viewpoint of SN 2010jl, a significant polarization could be observed because we are seeing the same geometry edge-on. Andrews et al. (2011) find a similar geometry with a torus inclined at 60°–80° for SN 2010jl, while Huk (2017b) finds an inclination angle of 51°–74°. Dessart et al. (2015) and Smith et al. (2011) also favour an edge-on view of SN 2010jl.

It is plausible that even if all SNe IIn are significantly asymmetric in either their explosion or CSM interaction, a number of SNe IIn would still exhibit low continuum polarization simply because of a viewing-angle effect. To date, no published studies of SNe IIn examined with spectropolarimetric data have shown little to no polarization (i.e. less than 1 per cent) until this study of SN 2014ab. It is therefore important to examine a larger population of SNe IIn with spectropolarimetric data to determine if a similar geometry but with different orientations could account for the distinctions seen in SN 2014ab compared to other more typical SNe IIn. Although we do not have early photometry to compare the rise of SN 2014ab to that of SN 2010jl and SNe IIn light curves are complicated by many factors involved in CSM interaction, Suzuki, Moriya & Takiwaki (2019) have suggested that differences in the viewing angle for SNe IIn would manifest themselves in the light curves of the SNe. Such attempts to understand the impact of viewing angle on the observable features of SN IIn should be continued. For instance, efforts to model the polarization of H α profiles of SNe IIn to better understand the importance of viewing angle (Huk 2017a) should be continued and expanded upon.

5 SUMMARY

SN 2014ab is unusual compared to most Type IIn SNe with published spectropolarimetry in that it exhibits very low detectable continuum polarization (0.07 per cent $\pm$ 0.04 per cent to 0.43 per cent $\pm$ 0.09 per cent, with an upper limit of $<$1.18 per cent, limited primarily by the uncertainty in the ISP) in all five epochs of spectropolarimetry, whereas all other SNe IIn with published polarization measurements show $>$1 per cent continuum polarization. Although this lack of polarization implies near-circular symmetry in the plane of the sky, the spectra of SN 2014ab display evidence for significant asymmetry along our line of sight based on radial velocities. Without spectropolarimetric data, we would have simply concluded that SN 2014ab was a typical asymmetric SN IIn without a constraint on our viewing angle. Thus, it is crucial that spectropolarimetric data, even if it results in very low polarization measurements, is obtained in order to better constrain physical parameters of SNe IIn. Below we summarize our main results.

(i) SN 2014ab was already on the decline when first detected, and with the last pre-detection upper limit 212 d before detection, the date of explosion for SN 2014ab is uncertain. Its observed peak was $M_V = -19.14$ mag at the time of first detection, but the true peak was likely somewhat brighter. It declined very slowly, maintaining a brightness comparable to that of superluminous SNe for over 200 d.

(ii) Our spectra cover roughly 150 d and we see little evolution in the spectral features during this time. This reinforces the conjecture that SN 2014ab was not first observed near its explosion date, but rather many weeks or months after explosion.

(iii) Narrow emission and absorption components of lines like H α and H β indicate an expansion speed of 80 km s^{-1} for the pre-shock CSM. This likely corresponds to the progenitor wind speed or expansion speed of a pre-SN eruption.

(iv) Based on the sustained luminosity of SN 2014ab, the intermediate-width component of its H α emission line from post-shock gas, and its CSM speed, we estimate the mass-loss rate of the SN 2014ab progenitor to be $\dot{M} \approx 1\,\mathrm{M}_\odot\,\mathrm{yr}^{-1}(v_\mathrm{w}/(80\,\mathrm{km\,s}^{-1}))$. From the roughly 200-d duration of the high-luminosity phase, combined with the relative speeds of the CSM and shock, we infer a total mass-loss of at least $\sim 5\,\mathrm{M}_\odot$ in the decade or so before explosion.

(v) We measure the continuum polarization of SN 2014ab at five different epochs spanning days 76 to 165 to be between

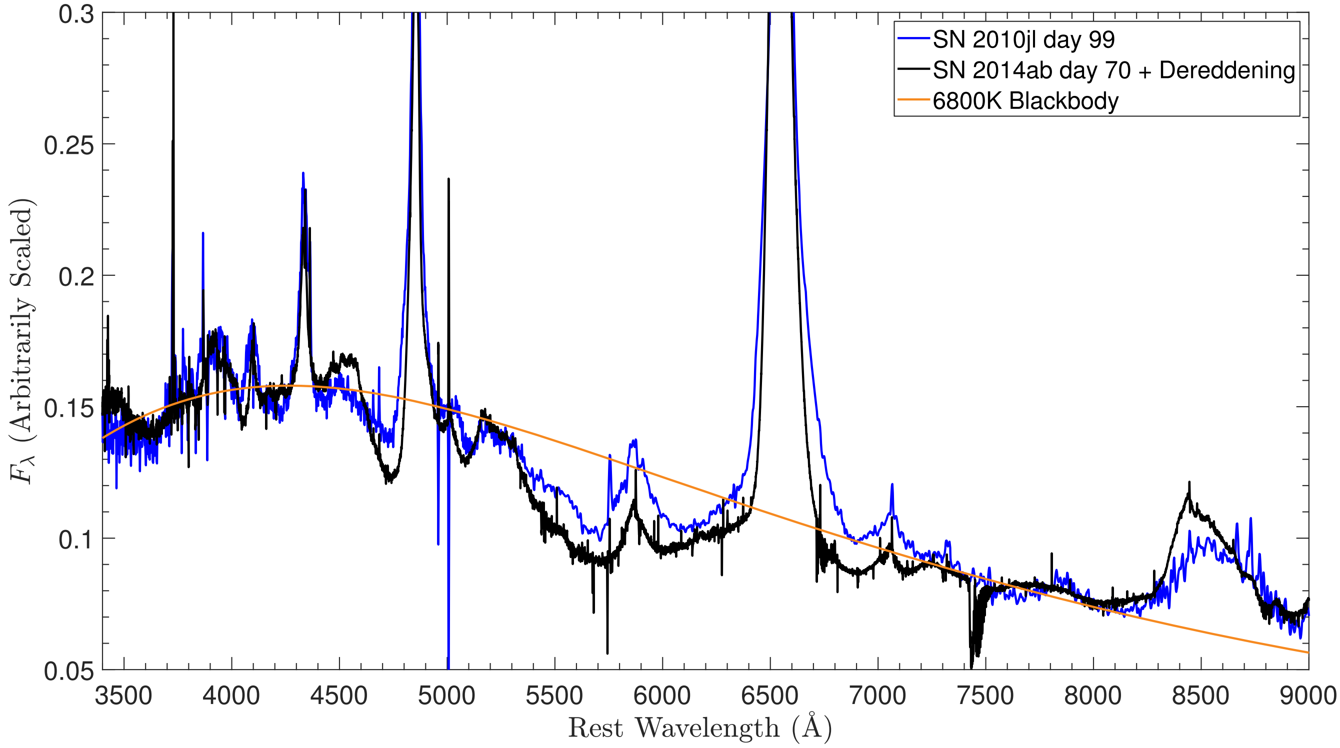

Figure 18. A comparison of the spectra for SN 2014ab (day 70, VLT X-shooter) and SN 2010jl (2014 February 9, Lick/Kast, Smith et al. 2012, corresponding to day 99) that have both been dereddened. This spectrum of SN 2014ab was dereddened by an additional amount $E_{B-V} = 0.10$ mag beyond the Milky Way and host-galaxy reddening applied earlier. This additional amount was chosen so that the continuum slope of SN 2014ab would match the continuum shape of SN 2010jl for comparison of their spectral features. We chose an SN 2010jl spectrum from a later relative date because the date of discovery for SN 2014ab was likely later relative to its peak. A 6400 K blackbody is shown in orange. The optical spectral features are remarkably similar in SN 2014ab and SN 2010jl, though SN 2014ab clearly exhibits stronger broad P-Cygni absorption features and a stronger Ca II near-IR triplet.

0.07 per cent $\pm$ 0.04 per cent and 0.43 per cent $\pm$ 0.09 per cent. The ISP dominates the uncertainty in the true polarization, providing an upper limit of 1.18 per cent. This suggests that SN 2014ab is not significantly polarized, unlike other SNe IIn with published spectropolarimetry to date showing 1–3 per cent continuum polarization.

(vi) Spectra of SN 2014ab indicate a number of interesting features. In particular, the H α and Pa β line profiles exhibit similar shape at all epochs, implying little or no small dust grain formation. Additionally, strong P-Cygni absorption is seen in H β extending out to $-18\,000$ km s^{-1}, suggesting that we are observing the continuum photosphere through a significant portion of the rapidly expanding SN ejecta.

(vii) Overall, SN 2014ab shows many similarities to SN 2010jl (see Fig. 18). Both SNe have asymmetric H α emission features with an intermediate-width component offset blueward of the narrow component. In the case of SN 2010jl, this asymmetric line profile evolves over time and is probably caused by dust formation (Smith et al. 2012; Gall et al. 2014), in contrast to SN 2014ab.

(viii) Importantly, SN 2014ab differs from SN 2010jl in a number of ways. Spectropolarimetry of SN 2014ab suggests lower continuum polarization. Spectra of SN 2014ab show broad P-Cygni absorption features probably arising in the fast SN ejecta, and Ca II near-IR triplet emission features stronger than those seen in SN 2010jl.

(ix) We suggest that SN 2014ab and SN 2010jl could have quite similar CSM geometry but are viewed from different directions. SN 2014ab may be viewed nearly along the axis of symmetry (i.e. from above the pole), yielding low polarization due to its symmetry in the plane of the sky but allowing us to directly see the fast polar SN ejecta, whereas SN 2010jl may be viewed near edge-on, revealing larger polarization levels and partly hiding the broad P-Cygni absorption features.

As our paper was in the final stages of preparation, a preprint appeared that presented an independent analysis of similar spectroscopic data on SN 2014ab (Moriya et al. 2020). We briefly note some similarities and differences in the two analyses here. Those authors similarly find SN 2014ab to be a luminous and slowly declining Type IIn SN with a blueshifted intermediate-width component in H α comparable to that of SN 2010jl. While Moriya et al. (2020) do not present polarization data (as we do), they utilize mid-IR observations (whereas we do not). Based on the mid-IR data, they suggest that SN 2014ab had pre-existing dust in the CSM, but did not have significant formation of dust in the cool dense shell as SN 2010jl did (Smith et al. 2012). We draw a similar conclusion about the lack of dust formation in SN 2014ab based on spectral line profiles. However, Moriya et al. (2020) argue that the blueshifted intermediate-width component of H α is symmetric, adequately fit by a Lorentzian, and can be explained by acceleration of the unshocked CSM by SN radiation. In contrast, we find that the intermediate-width line profile is not symmetric and cannot be fit by a Lorentzian, and requires either obscuration by large dust grains (because the effect is not strongly wavelength dependent), occultation by optically thick material, or a lack of symmetry between the far side and near side of the interaction region. Other than these points, our study and theirs find similar results.

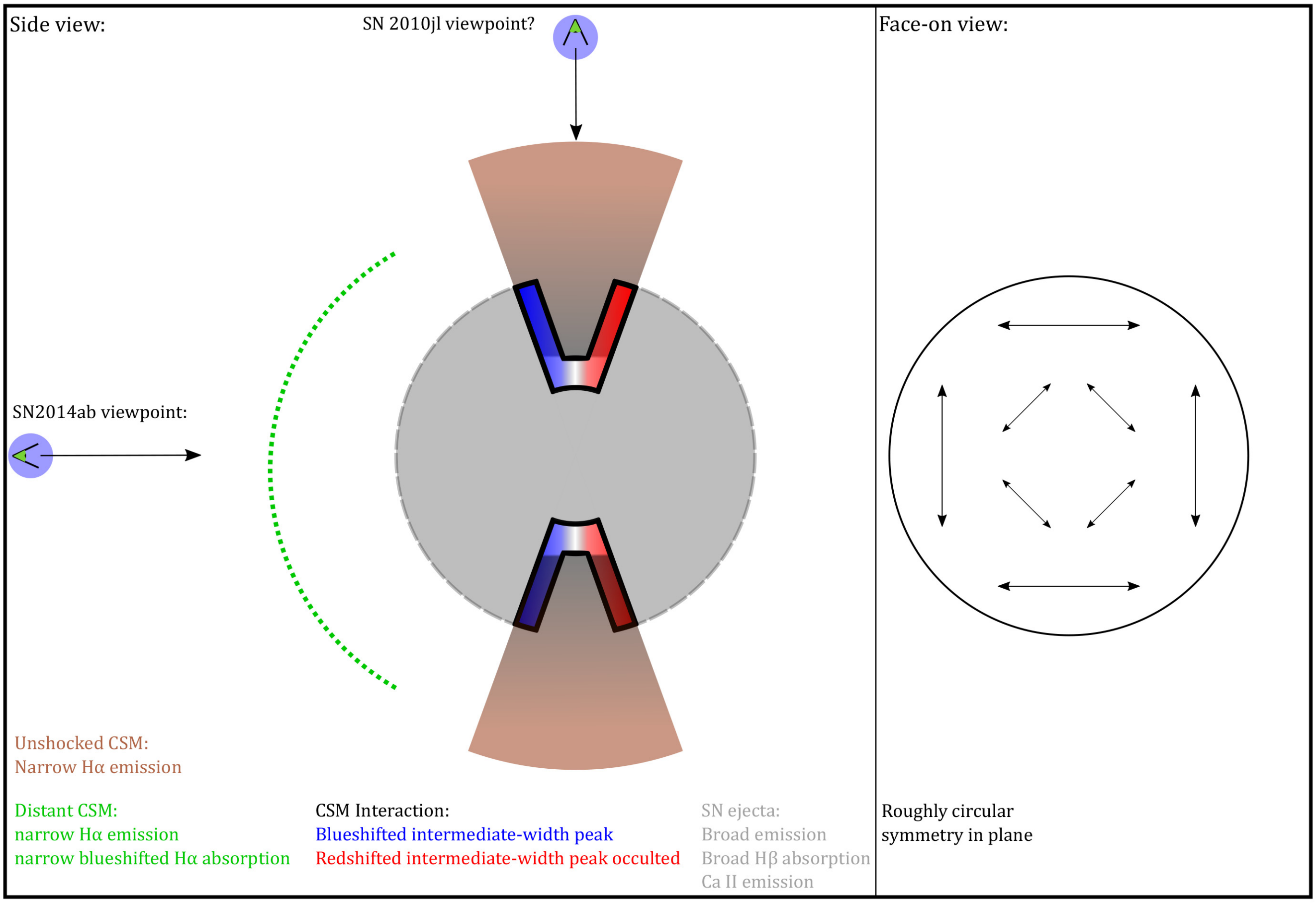

Figure 19. A schematic showing how the viewing angle may significantly impact what line features and polarization are observed in SNe IIn. The prominent Ca II near-IR triplet emission, broad H β absorption, and broad H α probably originate in the SN ejecta shaded in grey. The CSM interaction region outlined in black is likely the source of the asymmetric blueshifted intermediate-width peak of the H α line profile, because the continuum photosphere in this zone occults the redshifted side. The distant CSM shown in green causes the narrow blueshifted H α and H β absorption. Both the distant CSM in green and brown cause the narrow H α emission. These features suggest that the likely viewing angle for SN 2014ab is from above the pole or axis of symmetry (from the side as labelled above). For SN 2010jl, the observer may be seeing a similar geometry from a vantage point near the equatorial plane (from above in the schematic shown here). The spectropolarimetric data suggest we see a roughly circularly symmetric SN from a perpendicular viewpoint.

ACKNOWLEDGEMENTS

We thank the referee for their useful comments that have improved the manuscript. We thank Andrew Bigley, James Bradley, Kiera Fuller, Carolina Gould, Melissa L. Graham, Kevin Hayakawa, Minkyu Kim, Jon C. Mauerhan, and Isaac Shivvers for their assistance with some of the observations and reductions.

This work was supported by National Science Foundation (NSF) grant AST-1210599. NS received additional support from NSF grants AST-1312221 and AST-1515559, and by a Scialog grant from the Research Corporation for Science Advancement. DAH and GH were supported by NSF grant AST-1313484. Research by DJS was supported by NSF grants AST-1821967, 1821987, 1813708, 1813466, 1908972, and by the Heising-Simons Foundation under grant #2020-1864. The work of AVF's supernova group at U.C. Berkeley has been generously supported by NSF grant AST-1211916, the TABASGO Foundation, the Christopher R. Redlich Fund, and the Miller Institute for Basic Research in Science (U.C. Berkeley). DCL acknowledges support from NSF grants AST-1009571 and AST-1210311, under which part of this research was carried out. X-shooter observations collected at the European Southern Observatory under ESO programme 092.D-0645(A) and EFOSC2 observations collected at the European Southern Observatory under ESO programme 191.D-0935 were used in this work. This research used astrometric solutions from Astrometry.net. We also made use of the NASA/IPAC Extragalactic Database (NED), which is operated by the Jet Propulsion Laboratory, California Institute of Technology, under contract with NASA. This work makes use of observations from the Las Cumbres Observatory network.

We thank the staffs at the MMT, Bok, Lick, European Southern Observatories, and Las Cumbres Observatories for their assistance with the observations. Observations using Steward Observatory facilities were obtained as part of the large observing program AZTEC: Arizona Transient Exploration and Characterization. Some observations reported here were obtained at the MMT Observatory, a joint facility of the University of Arizona and the Smithsonian Institution. Research at Lick Observatory was partially supported by a generous gift from Google.

DATA AVAILABILITY

The data underlying this article will be shared on reasonable request to the corresponding author.

REFERENCES

Alard C., Lupton R. H., 1998, ApJ, 503, 325
Andrews J. E. et al., 2011, AJ, 142, 45
Andrews J. E., Smith N., McCully C., Fox O. D., Valenti S., Howell D. A., 2017, MNRAS, 471, 4047
Arcavi I. et al., 2014, ApJ, 793, 38
Bilinski C., Smith N., Li W., Williams G. G., Zheng W., Filippenko A. V., 2015, MNRAS, 450, 246
Bilinski C. et al., 2018, MNRAS, 475, 1104
Borish H. J., Huang C., Chevalier R. A., Breslauer B. M., Kingery A. M., Privon G. C., 2015, ApJ, 801, 7
Brown T. M. et al., 2013, PASP, 125, 1031
Buzzoni B. et al., 1984, The Messenger, 38, 9
Chevalier R. A., 2012, ApJ, 752, L2
Chugai N. N., Danziger I. J., 1994, MNRAS, 268, 173
Dessart L., Hillier D. J., Gezari S., Basa S., Matheson T., 2009, MNRAS, 394, 21
Dessart L., Audit E., Hillier D. J., 2015, MNRAS, 449, 4304
Drake A. J. et al., 2009, ApJ, 696, 870
Evans C. R., Kochanek C. S., 1989, ApJ, 346, L13
Faran T. et al., 2014a, MNRAS, 445, 554
Fassia A. et al., 2000, MNRAS, 318, 1093
Filippenko A. V., 1982, PASP, 94, 715
Filippenko A. V., 1997, ARA&A, 35, 309
Fransson C. et al., 2002, ApJ, 572, 350
Fransson C. et al., 2005, ApJ, 622, 991
Fransson C. et al., 2014, ApJ, 797, 118
Fraser M. et al., 2014, Astron. Telegram, No. 5968
Gall C. et al., 2014, Nature, 511, 326
Ganeshalingam M. et al., 2010, ApJS, 190, 418
Gezari S. et al., 2012, Nature, 485, 217
Hoffman J. L., et al., 2008, ApJ, 688, 1186
Howerton S. et al., 2014, Central Bureau Electronic Telegrams, 3826, 1
Huk L., 2017a, in Eldridge J. J., Bray J. C., McClelland L. A. S., Xiao L., eds, Proc. IAU Symp. 329, The Lives and Death-Throes of Massive Stars. Cambridge Univ. Press, Cambridge, p. 408
Huk L. N., 2017b, PhD thesis, University of Denver, p. 161
Katsuda S., Maeda K., Nozawa T., Pooley D., Immler S., 2014, ApJ, 780, 184
Kumar B. et al., 2019, MNRAS, 488, 3089
Lang D., Hogg D. W., Mierle K., Blanton M., Roweis S., 2010, AJ, 139, 1782
Leonard D. C., Filippenko A. V., Barth A. J., Matheson T., 2000, ApJ, 536, 239
Leonard D. C. et al., 2002b, PASP, 114, 35
Maeda K. et al., 2013, ApJ, 776, 5
Mauerhan J., Smith N., 2012, MNRAS, 424, 2659
Mauerhan J. et al., 2014, MNRAS, 442, 1166
Miller J. S., Stone R. P. S., 1993, Lick Obs. Tech. Rep. 66. Lick Obs., Santa Cruz
Moffat A. F. J., 1969, A&A, 3, 455
Moriya T. J. et al., 2020, preprint (arXiv:2006.10198)
Munari U., Zwitter T., 1997, A&A, 318, 269
Ofek E. O. et al., 2014, ApJ, 781, 42
Oke J. B., 1990, AJ, 99, 1621
Patat F., Taubenberger S., Benetti S., Pastorello A., Harutyunyan A., 2011, A&A, 527, LL6
Pei Y. C., 1992, ApJ, 395, 130
Phillips M. M. et al., 2013, ApJ, 779, 38
Phinney E. S., 1989, in Morris M., ed., Proc. IAU Symp. 136, The Center of the Galaxy. Kluwer, Dordrecht, p. 543
Poon H., Pun J. C. S., Lam T. Y., Qiu Y. L., Wei J. Y., 2011, preprint (arXiv:1109.0899)
Porter A. L. et al., 2016, ApJ, 828, 24
Poznanski D., Ganeshalingam M., Silverman J. M., Filippenko A. V., 2011, MNRAS, 415, L81
Poznanski D., Prochaska J. X., Bloom J. S., 2012, MNRAS, 426, 1465
Quataert E., Shiode J., 2012, MNRAS, 423, L92
Rees M. J., 1988, Nature, 333, 523
Reilly E., Maund J. R., Baade D., Wheeler J. C., Höflich P., Spyromilio J., Patat F., Wang L., 2017, MNRAS, 470, 1491
Richmond M. W., Treffers R. R., Filippenko A. V., Paik Y., Leibundgut B., Schulman E., Cox C. V., 1994, AJ, 107, 1022
Riess A. G. et al., 2005, ApJ, 627, 579
Schlafly E. F., Finkbeiner D. P., 2011, ApJ, 737, 103
Schlegel E. M., 1990, MNRAS, 244, 269
Schmidt G. D., Elston R., Lupie O. L., 1992, AJ, 104, 1563
Schmidt G. D., Stockman H. S., Smith P. S., 1992, ApJ, 398, L57
Serkowski K., Mathewson D. S., Ford V. L., 1975, ApJ, 196, 261
Smith N., 2014, ARA&A, 52, 487
Smith N., 2017, in Alsabti A.W., Murdin P., eds, Handbook of Supernovae. Springer International Publishing, Berlin, p. 403
Smith N., McCray R., 2007, ApJ, 671, L17
Smith N., Arnett W. D., 2014, ApJ, 785, 82
Smith N., Owocki S. P., 2006, ApJ, 645, L45
Smith N. et al., 2007, ApJ, 666, 1116
Smith N., Chornock R., Li W., Ganeshalingam M., Silverman J. M., Foley R. J., Filippenko A. V., Barth A. J., 2008, ApJ, 686, 467
Smith N. et al., 2009, ApJ, 695, 1334
Smith N. et al., 2011, ApJ, 732, 63
Smith N., Silverman J. M., Filippenko A. V., Cooper M. C., Matheson T., Bian F., Weiner B. J., Comerford J. M., 2012, AJ, 143, 17
Smith N. et al., 2015, MNRAS, 449, 1876
Stahl B. E. et al., 2019, MNRAS, 490, 3882
Stetson P. B., 1987, PASP, 99, 191
Stritzinger M. et al., 2012, ApJ, 756, 173
Strubbe L. E., Quataert E., 2009, MNRAS, 400, 2070
Suzuki A., Moriya T. J., Takiwaki T., 2019, ApJ, 887, 249
Turatto M., Benetti S., Cappellaro E., 2003, in Hillebrandt W., Leibundgut B., eds, ESO Astrophys. Symp., From Twilight to Highlight: The Physics of Supernovae. Springer-Verlag, Berlin, p. 200
Ulrich M.-H., Maraschi L., Urry C. M., 1997, ARA&A, 35, 445
Vernet J. et al., 2011, A&A, 536, A105
Vorontsov-Velyaminov B. A., 1959, Atlas and Catalog of Interacting Galaxies, Sternberg Institute, Moscow State University
Wang L., Wheeler J. C., Höflich P., 1997, ApJ, 476, L27
Wang L., Howell D. A., Höflich P., Wheeler J. C., 2001, ApJ, 550, 1030
Woosley S. E., 2017, ApJ, 836, 244
Zhang T. et al., 2012, AJ, 144, 131

This paper has been typeset from a TEX/LATEX file prepared by the author.